

## META-ANALYSIS OF CRYOGENIAN THROUGH MODERN QUARTZ MICROTEXTURES REVEALS SEDIMENT TRANSPORT HISTORIES

JOCELYN N. REAHL,<sup>\*1</sup> MARJORIE D. CANTINE,<sup>\*\*1</sup> JULIA WILCOTS,<sup>1</sup> TYLER J. MACKEY,<sup>†1</sup> AND KRISTIN D. BERGMANN<sup>1</sup>

<sup>1</sup>*Massachusetts Institute of Technology, Department of Earth, Atmospheric, and Planetary Sciences, Cambridge, Massachusetts 02139, U.S.A.  
e-mail: jreahl@caltech.edu*

**ABSTRACT:** Quantitative analysis of quartz microtextures by means of scanning electron microscopy (SEM) can reveal the transport histories of modern and ancient sediments. However, because workers identify and count microtextures differently, it is difficult to directly compare quantitative microtextural data analyzed by different workers. As a result, the defining microtextures of certain transport modes and their probabilities of occurrence are not well constrained. We used principal-component analysis (PCA) to directly compare modern and ancient aeolian, fluvial, and glacial samples from the literature with nine new samples from active aeolian and glacial environments. Our results demonstrate that PCA can group microtextural samples by transport mode and differentiate between aeolian transport and fluvial and glacial transport across studies. The PCA ordination indicates that aeolian samples are distinct from fluvial and glacial samples, which are in turn difficult to disambiguate from each other. Ancient and modern sediments are also shown to have quantitatively similar microtextural relationships. Therefore, PCA may be a useful tool to constrain the ambiguous transport histories of some ancient sediment grains. As a case study, we analyzed two samples with ambiguous transport histories from the Cryogenian Bråvika Member (Svalbard). Integrating PCA with field observations, we find evidence that the Bråvika Member facies investigated here includes aeolian deposition and may be analogous to syn-glacial Marinoan aeolian units including the Bakoye Formation in Mali and the Whyalla Sandstone in South Australia.

### INTRODUCTION

Quantitative analysis of quartz microtextures by means of scanning electron microscopy (SEM) reveals microscale features (microtextures) that are formed during transport (Krinsley and Takahashi 1962; Krinsley and Doornkamp 1973; Bull 1981). Because different transport modes imprint specific suites of microtextures onto quartz grains, quartz microtextural analysis is a useful technique to understand the transport histories of modern and ancient sedimentary deposits (Krinsley and Doornkamp 1973; Mahaney 2002; Vos et al. 2014). Quantitative quartz microtextural analysis, which treats microtextural data as a multidimensional statistical problem, is a particularly promising method to quantify the probabilities of occurrence of each microtexture in a specific transport mode (Mahaney et al. 2001; Řiha et al. 2019). However, because workers identify and count microtextures differently—even for sand grains from the same depositional environment (Culver et al. 1983)—it is difficult to directly compare quantitative microtextural data analyzed by more than one worker in the same reference frame.

Here we use principal-component analysis (PCA) to directly compare quantitative microtextural data from modern and ancient aeolian, fluvial,

and glacial sediments across workers. Because experimental studies have shown that certain microtextures form in specific transport settings (Krinsley and Takahashi 1962; Lindé and Mycielska-Dowgiallo 1980; Costa et al. 2012, 2013, 2017), we expect the PCA ordinations to distinguish aeolian, fluvial, and glacial sediments from each other regardless of worker. We also hypothesize that the modern and ancient samples will be quantitatively similar to each other in PCA space, and that the depositional histories of ambiguous ancient sedimentary environments can be constrained using this method.

One such case of an ambiguous ancient sedimentary environment is the Cryogenian (720–635 Ma) Bråvika Member (northeastern Svalbard, Norway). The Bråvika Member is a northward-thickening and coarsening-upward wedge of quartz arenite with lenses and beds of dolomite (Halverson et al. 2004). Since the Bråvika Member was first recognized as a unit by Halverson et al. (2004), there have been three prevailing hypotheses for what depositional environment the Bråvika could represent:

- 1) a glaciofluvial outwash plain associated with the overlying Wilsonbreen Formation (Halverson et al. 2004), which is correlated with the Marinoan “Snowball Earth” pan-glaciation (Hoffman et al. 2012);
- 2) an aeolian depositional environment associated with either the glacial conditions of the Wilsonbreen Formation or the tropical equatorial conditions of the underlying upper Elbobreen Formation (Halverson 2011), the latter of which is correlated with the Cryogenian interglacial period (Fairchild et al. 2016); or

\* Present Address: California Institute of Technology, Division of Geological and Planetary Sciences, Pasadena, California 91125, U.S.A.

\*\* Present Address: Institut für Geowissenschaften, Goethe-Universität, Altenhöferallee 1, 60438 Frankfurt am Main, Germany

† Present Address: University of New Mexico, Department of Earth and Planetary Sciences, Albuquerque, New Mexico 87131, U.S.A.

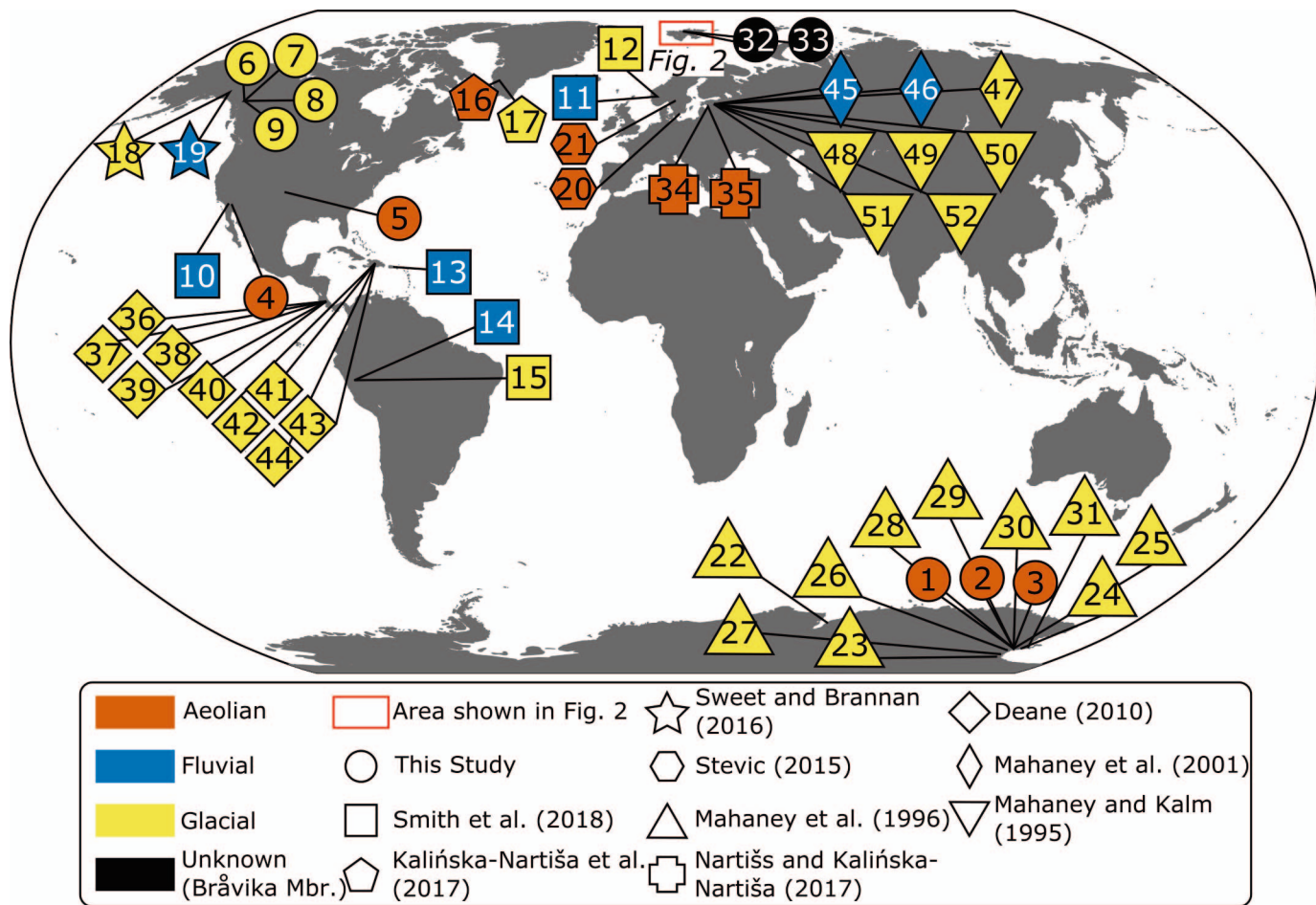


FIG. 1.—Global map of all samples analyzed in this study. The number in each marker corresponds to the sample group number in Tables 1 and 2.

3) a tropical fluvial environment associated with the upper Elbobrene Formation (Hoffman et al. 2012).

To test if our PCA analysis method can constrain the transport histories of ambiguous ancient sedimentary environments, we transformed two microtextural samples of the Bråvika Member from Buldrevågen (northeast Spitsbergen) into the PCA ordinations. Integrating the microtextural data with field observations from Buldrevågen, Geerabukta (Ny Friesland), and Gimleodden (Nordaustlandet), we show that PCA is not only able to distinguish aeolian, fluvial, and glacial transport modes from each other using microtextural data, but it is also able to help elucidate the ambiguous transport histories of ancient sediment grains.

## MATERIALS

### Modern Samples

**New Modern Samples.**—We present five new aeolian samples from the McMurdo Dry Valleys (Antarctica), Algodones Dunes of California (Cocopah (*Kwapa*), Kumeyaay, Salt River Pima–Maricopa (*O'odham-Piipaash*), and Quechan (*Kwatsáan*) territory), and Waynoka Dunes of Oklahoma (Comanche (*Nánumuñu*), Keechi (*Ki:che:ss*), Kiowa (*Gáui/dòñ:gyà*), Osage (*Wahzhazhe*), Tawakoni (*Tawá:kharih*), Waco (*Wí:ko?*), and Wichita (*Kirkir?i:s*) territory), as well as four new glacial samples from the Llewellyn Glacier in British Columbia on Taku River Tlingit (*Lingít*) territory (Fig. 1; Table 1). Each of these samples are briefly

described in the following paragraphs, and more detailed descriptions can be found in the Supplemental Material.

Of the five aeolian samples, three are sourced from perennially ice-covered lakes in the McMurdo Dry Valleys: one from Lake Fryxell (documented in Jungblut et al. 2016), one from Lake Joyce (documented in Mackey et al. 2015), and one from Lake Vanda (documented in Mackey et al. 2017). The bulk of coarse-grained sedimentation under the ice cover of these lakes is wind-blown quartz- and feldspar-rich sand that melts through the ice and is deposited within layers of microbial mats on the lake floor (Gumbley 1975; Green et al. 2004; Shacat et al. 2004; Jungblut et al. 2016). The lakes' lack of wind-driven turbulence (Spigel and Priscu 1998) and neutral to high pH (Green et al. 2004; Shacat et al. 2004; Jungblut et al. 2016) suggest that these aeolian grains are negligibly overprinted by lacustrine transport or acidification processes after they melt through the ice.

The remaining two aeolian samples are from the Algodones Dunes and the Waynoka Dunes (both documented by Adams 2018; Adams and Soreghan 2020). Both dunefields are sourced from fluvial deposits (Winspear and Pye 1995; Lepper and Scott 2005) and have been active since the late Holocene (Stokes et al. 1997; Lepper and Scott 2005). Given that aeolian transport over short distances and timeframes rapidly imprints aeolian microtextures on quartz grains (Costa et al. 2013), we expect there to be negligible fluvial overprinting on these samples.

The four glacial samples from the Llewellyn Glacier on the Juneau Icefield were collected from lateral glacial moraines (JIF19-C26-02 and JIF19-C26-03) and an ephemeral glaciofluvial melt stream 10 m

TABLE 1.—List of the samples from modern depositional environments considered in this study. Each group of samples is assigned a number for later reference in Figures 1 and 5 (Column #). Column S indicates the number of samples in each sample group, and column N indicates the number of quartz grains in each sample group.

Study	#	Sample Location	Transport	S	N	GPS Point
This Study	1	Lake Fryxell, McMurdo Dry Valleys, Antarctica	Aeolian	1	31	77°36'48"S, 163°06'40"E
	2	Lake Joyce, McMurdo Dry Valleys, Antarctica	Aeolian	1	34	77°43'11"S, 161°36'25"E
	3	Lake Vanda, McMurdo Dry Valleys, Antarctica	Aeolian	1	30	77°31'38"S, 161°36'24"E
	4	Algodones Dunes, California, U.S.	Aeolian	1	44	33°08'57"N, 115°18'48"W
	5	Waynoka Dunes, Oklahoma, U.S.	Aeolian	1	48	36°33'35"N, 98°53'56"W
	6	Llewellyn Glacier, B.C. (JIF19-C26-01)	Glacial	1	31	59°00'49"N, 134°07'15"W
	7	Llewellyn Glacier, B.C. (JIF19-C26-02)	Glacial	1	39	59°00'48"N, 134°07'13"W
	8	Llewellyn Glacier, B.C. (JIF19-C26-03)	Glacial	1	36	59°00'48"N, 134°07'13"W
	9	Llewellyn Glacier, B.C. (JIF19-C26-04)	Glacial	1	40	59°00'50"N, 134°07'14"W
Smith et al. (2018)	10	Anza-Borrego Desert, California, U.S.	Fluvial	5	250	32°54'00"N, 116°16'00"W
	11	Auster and Storelv Rivers, Norway	Fluvial	7	346	61°32'00"N, 06°57'00"E
	12	Austerdal Glacier Moraine, Norway	Glacial	1	50	61°32'00"N, 06°57'00"E
	13	Rio Guayanés, Puerto Rico	Fluvial	6	297	18°03'00"N, 65°54'00"W
	14	Rio Parón, Peru	Fluvial	5	250	09°00'00"S, 77°42'00"W
Kalińska-Nartša et al. (2017)	15	Moraine Proximal to Lake Parón, Peru	Glacial	1	48	09°00'00"S, 77°42'00"W
	16	Russell Glacier, Greenland (CE1, CE2, CE8)	Aeolian	3	60	67°05'00"N, 50°20'00"W
	17	Russell Glacier, Greenland (CE12, CE13)	Glacial	2	40	67°07'00"N, 50°05'00"W
Sweet and Brannan (2016)	18	Chitina Glacier Moraine to 12 km Past Tana River Confluence, Alaska, U.S. (CR-1 to CR-23)	Glacial	22	626	61°05'44"N, 142°11'03"W
	19	12 km Past Tana River Confluence to the Copper River, Alaska, U.S. (CR-24 to CR-41)	Fluvial	18	450	61°21'42"N, 143°46'34"W
Stevic (2015)	20	Coastal Sand Dune, Vittskövle, Sweden	Aeolian	1	15	55°51'56"N, 14°10'02"E
	21	Inland Sand Dune, Brattforsheden, Sweden	Aeolian	1	15	59°36'26"N, 13°53'03"E
Mahaney et al. (1996)	22	Lichen Valley, Vestfold Hills, Antarctica (Site A)	Glacial	1	25	68°28'53"S, 78°10'24"E
	23	Ackerman Ridge, Scott Glacier area, Antarctica (Sites B – C)	Glacial	1	25	85°45'00"S, 153°00'00"W
	24	Southern Inexpressible Island, Antarctica (Site D)	Glacial	1	25	74°54'00"S, 163°39'00"E
	25	Taylor Glacier, McMurdo Dry Valleys, Antarctica (Site E)	Glacial	1	25	77°44'00"S, 162°10'00"E
	26	Hatherton Glacier, Antarctica (Site F)	Glacial	1	25	79°55'00"S, 157°35'00"E
	27	Roberts Massif, Antarctica (Sites G – H)	Glacial	2	50	85°32'00"S, 177°05'00"W
	28	Barwick Valley, Antarctica (Site I)	Glacial	1	25	77°23'24"S, 161°02'18"E
	29	Cambridge Glacier, Antarctica (Site J)	Glacial	1	25	76°57'00"S, 160°31'00"E
	30	Southern Inexpressible Island, Antarctica (Site D)	Glacial	1	25	75°38'00"S, 161°05'00"E
	31	Luther Peak Basin, Edisto Inlet, Antarctica (Site L)	Glacial	1	25	72°22'00"S, 169°50'00"E

downstream from a separated branch of ice from the Llewellyn Glacier (JIF19-C26-01 and JIF19-C26-04; Fig. S1, see Supplemental Material). Because many kilometers of fluvial transport are needed to create a fluvial microtextural overprint on glacial sediment (Pippin 2016; Sweet and Brannan 2016; Křížek et al. 2017), samples JIF19-C26-01 and JIF19-C26-04 are more representative of a glacial setting than a fluvial setting.

**Modern Literature Samples.**—Previously published aeolian, fluvial, and glacial samples comprise the remainder of modern samples considered in this study (Fig. 1; Table 1). We selected five studies to use in this modern dataset: Mahaney et al. (1996), Stevic (2015), Sweet and Brannan (2016), Kalińska-Nartša et al. (2017), and Smith et al. (2018).

Mahaney et al. (1996) analyzed 11 glacial samples distributed around the Antarctic continent. Stevic (2015) analyzed two aeolian samples, one from a coastal dune in Vittskövle, Sweden, and another from an inland sand dune near Brattforsheden, Sweden. Sweet and Brannan (2016) investigated the microtextural transition from glacially dominated samples to fluvially dominated ones using 46 samples of sand collected along a transect from the Chitina Glacier to the Copper River in Alaska. For the purposes of sorting these samples into *glacial* and *fluvial* bins, we use Sweet and Brannan's (2016) five-point averaged fluvial–glacial (F/G) microtextural ratio. Samples with a five-point averaged F/G > 1 are classified as *fluvial* samples, and samples with a five-point averaged F/G < 1 are classified as *glacial*. Kalińska-Nartša et al. (2017) analyzed three aeolian samples and two glacial samples from the Russell Glacier in

southwest Greenland. Finally, Smith et al. (2018) analyzed 25 fluvial and glacial samples from the Anza–Borrego Desert in California, the Auster and Storelv rivers in Norway, the Rio Guayanés in Puerto Rico, and the Rio Parón in Peru. Because Smith et al. (2018) saw no significant change in percussion features along each of the river transects—even in glaciofluvial settings—the *fluvial* samples in Smith et al. (2018) are defined as those collected along river transects and the *glacial* samples are defined as those collected at moraines.

#### Ancient Samples

**Cryogenian Bråvika Member, Svalbard, Norway.**—We analyzed two samples of the Bråvika Member from a site at Buldrevågen in north-northeast Spitsbergen (Fig. 2), one at 12 m and another at 22 m above the base of the Bråvika Member. We will present field observations of the Bråvika Member from outcrops in Buldrevågen, Geerabukta (Ny Friesland), and Gimleodden (Nordaustralandet) as context for the microtextural samples.

The Cryogenian Bråvika Member is a northward-thickening and coarsening-upward wedge of quartz arenite with lenses and beds of dolomite that crop out in northeastern Svalbard, Norway (Halverson et al. 2004). The Bråvika Member is situated between two units that are interpreted to represent different Cryogenian climate states (Fig. 2). The underlying siltstone and dolomite of the upper Elbobreen Formation (MacDonaldryggen and Slangen members) are correlated with the warm Cryogenian interglacial period (Fairchild et al. 2016), which spanned from

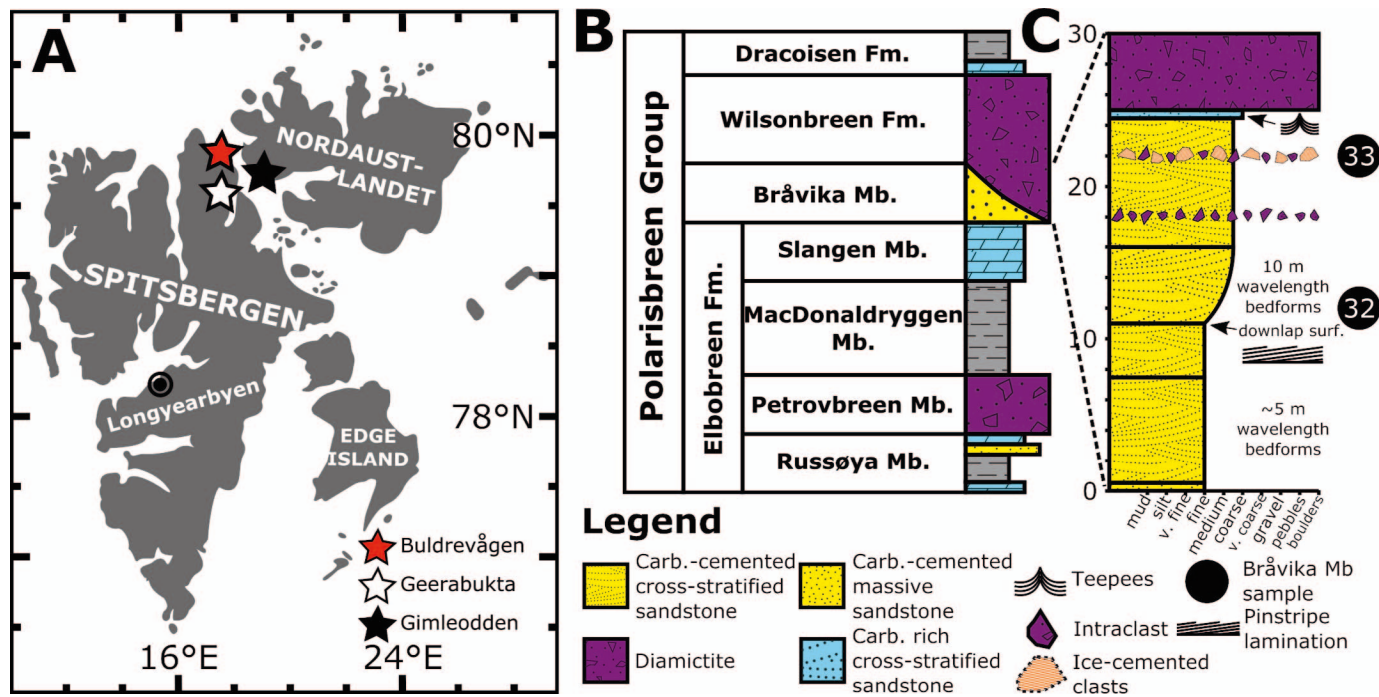


FIG. 2.—Geologic context and stratigraphy of the Cryogenian Bråvika Member in Svalbard. A) Map of the Svalbard archipelago. Each star indicates a site observed in this study: Buldrevågen (red), Geerabukta (white), and Gimleodden (black). B) Generalized stratigraphic nomenclature for the Cryogenian Polarisbreen Group in Svalbard after Halverson et al. (2018). As shown here, the Bråvika Member is assigned to neither the Wilsonbreen nor the Ellobreen formations, as its assignment is a key question explored in this study. The Petrovbrean Member is correlated with the Sturtian pan-glaciation and the Wilsonbreen Formation is correlated with the Marinoan pan-glaciation. The MacDonaldryggen and Slangen members are correlated with the Cryogenian interglacial (Fairchild et al. 2016). C) Stratigraphic column of the Bråvika Member at Buldrevågen. The black circles indicate where samples 32 (J1701-156) and 33 (J1701-166) were collected for microtextural analysis.

the Sturtian deglaciation to the Marinoan glacial initiation. Absolute age constraints on this period are limited, but the Sturtian deglaciation is constrained between  $> 662.7 \pm 6.2$  Ma (U-Pb SIMS in South China; Yu et al. 2017) to  $> 657.2 \pm 2.4$  Ma (Re-Os in southern Australia; Kendall et al. 2006), and the Marinoan glacial onset is constrained between  $< 654.6 \pm 3.8$  Ma (U-Pb SIMS in South China; Zhang et al. 2008) to  $> 639.29 \pm 0.26/0.31/0.75$  Ma (U-Pb CA-ID-TIMS in Congo; Prave et al. 2016). The overlying glacial diamictites of the Wilsonbreen Formation share a reciprocal thickness relationship with the Bråvika Member and are correlated with the Marinoan glaciation (Hoffman et al. 2012), which ended between  $636.41 \pm 0.45$  Ma (U-Pb CA-ID-TIMS in Southern Australia; Calver et al. 2013) and  $635.2 \pm 0.6$  Ma (U-Pb zircon in South China; Condon et al. 2005).

**Ancient Literature Samples.**—In addition to the two Bråvika Member samples, we compiled a set of ancient aeolian, fluvial, and glacial microtextural samples from four studies: Mahaney and Kalm (1995), Mahaney et al. (2001), Deane (2010), and Nartišs and Kalińska-Nartiša (2017) (Fig. 1; Table 2).

Mahaney and Kalm (1995) analyzed 23 glacial samples from the Pleistocene Dainava, Ugandi, Varduva, and Latvia tills in Estonia. Mahaney et al. (2001), following Mahaney and Kalm (2000), used quantitative microtextural analysis and Euclidian distances to characterize 29 Pleistocene glacial samples, three Pleistocene glaciogenic samples, and 21 Middle Devonian fluvial samples from Estonia. All of these samples were previously collected and analyzed in Mahaney and Kalm (2000). Deane (2010) compared nine Last Glacial Maximum (LGM) glaciogenic samples from Costa Rica with nine potentially glaciogenic samples from the Dominican Republic and found that the two sample sets were statistically indistinguishable, supporting a glaciogenic history for the

samples from the Dominican Republic. In our study, we include samples from Deane (2010) that were collected directly from known or hypothesized glacial diamictites and moraines in Costa Rica and the Dominican Republic; we did not include samples from glaciolacustrine environments and debris flows. Nartišs and Kalińska-Nartiša (2017) analyzed two aeolian samples from periglacial aeolian dunes associated with the retreat of the Fennoscandian ice sheet after the LGM in Latvia.

## METHODS

### Field Work and Sample Collecting

Samples analyzed for the first time in this study were collected over multiple field seasons using a variety of methods. The samples from the McMurdo Dry Valleys were originally collected as microbial mats using the methods described in Mackey et al. (2015), Jungblut et al. (2016), and Mackey et al. (2017). Samples from the Algodones Dunes and Waynoka Dunes were collected using the methods described in Adams and Soreghan (2020). On the Juneau Icefield, four sand samples of  $\sim 50$  g each were collected in August 2019 from glacial moraines and an ephemeral glaciogenic melt stream on the Llewellyn Glacier (Camp 26) nunatak. Field work on the Bråvika Member in Buldrevågen, Geerabukta, and Gimleodden was performed in 2017.

### Microtextural Sample Disaggregation and SEM Preparation

Most samples collected for this study were unconsolidated sediment, but consolidated samples were disaggregated before analysis. Both dolomite-cemented Bråvika Member samples from Svalbard were disaggregated using 1N hydrochloric acid (HCl) at 50°C for 24 hours. Sand samples from Lake Joyce, Lake Fryxell, and Lake Vanda were disaggregated from the

TABLE 2.—List of the samples from ancient depositional environments considered in this study. Each group of samples is assigned a number for reference in Figures 1, 2, and 6 (Column #). Column S indicates the number of samples in each sample group, and column N indicates the number of quartz grains in each sample group.

Study	#	Sample	Transport	S	N	GPS Point	Geologic Period
This Study	32	Bråvika Mbr., Buldrevågen (J1701-156)	Unknown	1	39	79°59'29"N, 17°31'20"E	Cryogenian
	33	Bråvika Mbr., Buldrevågen (J1701-166)	Unknown	1	40	79°59'29"N, 17°31'20"E	
Nartišs and Kalińska-Nartiša (2017)	34	Middle Gauja Lowland, Latvia (Mielupīte 1.3)	Aeolian	1	16	57°30'00"N, 26°00'00"E	Pleistocene
	35	Middle Gauja Lowland, Latvia (Mielupīte 1.7)	Aeolian	1	18	57°30'00"N, 26°00'00"E	
Deane (2010)	36	Till, Costa Rica (Sample 2)	Glacial	1	300	09°29'35"N, 83°29'07"W	Pleistocene
	37	Till, Costa Rica (Sample 3)	Glacial	1	100	09°29'35"N, 83°29'07"W	
	38	Till, Costa Rica (Sample 4)	Glacial	1	100	09°29'35"N, 83°29'07"W	
	39	Till, Costa Rica (Sample 5)	Glacial	1	100	09°29'35"N, 83°29'07"W	
	40	Till, Costa Rica (Sample 8)	Glacial	1	100	09°29'35"N, 83°29'07"W	
	41	Till, Dominican Republic (Sample 10)	Glacial	1	100	19°02'01"N, 71°04'22"W	
	42	Till, Dominican Republic (Sample 11)	Glacial	1	100	19°01'60"N, 71°04'26"W	
	43	Till, Dominican Republic (Sample 17)	Glacial	1	100	19°02'07"N, 71°04'38"W	
	44	Till, Dominican Republic (Sample 18)	Glacial	1	100	19°01'39"N, 71°02'30"W	
Mahaney et al. (2001)	45	Arküla Stage Sandstone, Estonia	Fluvial	21	420	58°15'00"N, 26°30'00"E	Middle Devonian
	46	Glaciofluvial Sand, Estonia	Fluvial	3	60	58°15'00"N, 26°30'00"E	Pleistocene
Mahaney and Kalm (1995)	47	Till, Estonia	Glacial	29	580	58°15'00"N, 26°30'00"E	
	48	Latvia Till, Estonia	Glacial	5	100	58°13'28"N, 26°25'16"E	Pleistocene
	49	Varduva Till, Estonia	Glacial	5	100	58°13'28"N, 26°25'16"E	
	50	Upper Ugandi Till, Estonia	Glacial	5	100	58°13'28"N, 26°25'16"E	
	51	Lower Ugandi Till, Estonia	Glacial	5	100	58°13'28"N, 26°25'16"E	
	52	Upper Dainava Till, Estonia	Glacial	3	60	58°13'28"N, 26°25'16"E	

microbial mats using 30% hydrogen peroxide ( $H_2O_2$ ) solution at 50°C for 24 hours to remove organics and 1N HCl at 50°C for 24 hours to remove carbonate.

All of the samples were then prepared for blind microtextural analysis in the style of Smith et al. (2018). Samples were distributed into vials and given unique codes unknown to the primary researcher. These blinded conditions were maintained until after each sample's microtextural data were collected.

After sample randomization, each sample was gently wet sieved into a 125  $\mu m$ –1 mm grain-size fraction and dried in an oven. After drying, the samples were treated with 30%  $H_2O_2$  solution at 50°C for 24 hours to remove organics. Samples were then treated with 1N HCl solution for 24 hours at 50°C to remove any remaining carbonate coatings. Neither  $H_2O_2$  nor low-concentration HCl at these temperatures and time frames affects quartz microtextures (Pye 1983; Keiser et al. 2015; Smith et al. 2018).

Samples were then treated using the citrate-bicarbonate-dithionite (CBD) method (Janitzky 1986) to remove iron-oxide and manganese-oxide coatings. Between all chemical treatments, the samples were thoroughly rinsed and dried. These samples were not sonicated, to prevent artificially inducing microtextures (Porter 1962).

Following these treatments, 50 grains that appeared to be quartz (e.g., translucent, no obvious cleavage, etc.) were randomly selected from each sample for microtextural analysis using a reflected-light microscope. The selected grains were mounted on an aluminum SEM stub with double-sided carbon tape in a 10  $\times$  5 grid and then coated with a 5 nm thick platinum–palladium alloy (Pt/Pd; 80/20) sputter coating to prevent charging under the SEM. Although a gold (Au) or gold–palladium alloy (Au/Pd) coating is frequently used for SEM samples (Vos et al. 2014), Pt/Pd is a better alternative to Au coatings because Pt/Pd coatings have a smaller grain size that permits higher-resolution analysis (5–10 nm Au vs. 4–8 nm Au/Pd vs. 2–3 nm Pt/Pd; Goldstein et al. 1992).

#### SEM Imaging and Analysis

All grains in each sample were photographed at a 30° tilt on a Zeiss FESEM Supra55VP using a secondary electron (SE2) detector at 20 kV EHT. Viewing the grains at a 30° angle helps to identify smaller

microtextures that are difficult to identify at a 0° angle (Margolis and Krinsley 1971). During imaging, energy-dispersive spectroscopy (EDS) was used to confirm the composition of each quartz grain.

After imaging, each quartz grain was analyzed for the presence or absence of 20 microtextures (Fig. 3) according to the methods of Mahaney et al. (2001) and Mahaney (2002). The microtextures are grouped into five bins as defined by Sweet and Soreghan (2010) that differentiate features by formation process: polygenetic, percussion, high-stress, chemical, and grain relief. The following formation descriptions are from Sweet and Soreghan (2010). Polygenetic features are formed through a variety of processes. Percussion features are formed via grain saltation. High-stress features are formed when grains are subjected to high shear stresses. Chemical features are formed via silica dissolution or precipitation. Grain relief refers to the difference between the high and low points on the grain surface.

Grains with extreme diagenetic overprint (e.g., greater than or equal to approximately 90% estimated coverage of diagenetic overprint; Fig. S2) were removed from the sample dataset. The probability of occurrence for each microtexture  $p_m$  was calculated by dividing the sum of the counts for a given microtexture by the total number of grains in the sample (Smith et al. 2018).

Previous microtextural studies have used a range of sample sizes, from less than 20 grains per sample (Krinsley and Funnell 1965; Coch and Krinsley 1971; Blackwelder and Pilkey 1972) to 100 grains or more per sample (Vincent 1976; Setlow 1978; Deane 2010). This study analyzed  $\leq 50$  grains per sample as a midpoint between these. However, non-quartz grains and diagenetically overprinted grains were removed from the sample dataset, making 50 grains the upper limit for samples in this study. To address this, samples with  $\geq 15$  eligible quartz grains were considered statistically significant for analysis; samples with  $< 15$  eligible quartz grains were not analyzed. This limit of 15 grains was selected because it is the midpoint of the lower limit recommended sample sizes of Costa et al. (2012), who advocated for a median number of 20 grains per sample, and of Vos et al. (2014), who advocated for a lower limit of 10 grains per sample.

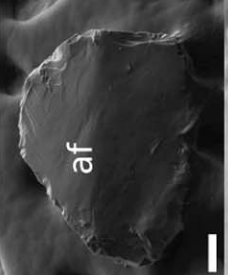
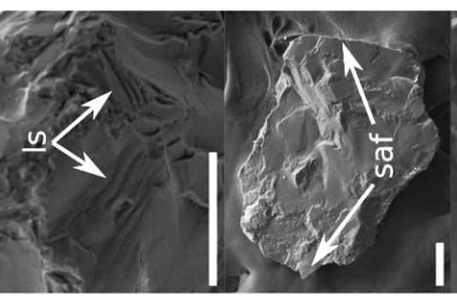
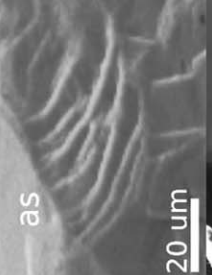
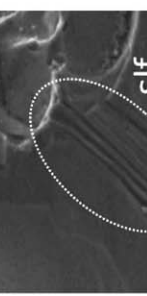
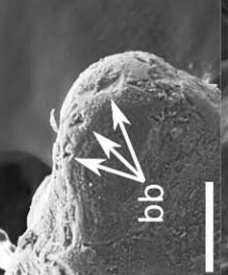
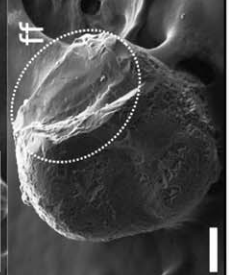
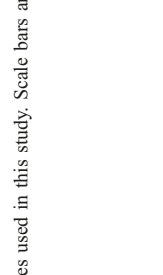
Microtexture	Abbr.	Description	Formation Process	Example Photo	Microtexture	Abbr.	Description	Formation Process	Example Photo
Abrasion Features	af	Rubbed or worn surface	Polygenetic		Linear Steps	ls	Widely spaced linear features, typically > 5 μm apart	Polygenetic	
Arc-Shaped Steps	as	Several microns deep and typically spaced > 5 μm apart	Polygenetic		Sharp Angular Features	saf	Distinct sharp edges on grain surface	Polygenetic	
Breakage Blocks	bb	Blocky void marking removal of material, typically along an edge	Polygenetic		Subparallel Linear Fractures	slf	Linear fractures, typically < 5 μm spacing	Polygenetic	
Conchoidal Fractures	cf	Smooth, curved fracture	Polygenetic		Edge Rounding	er	Rounded edges on grains	Percussion	
Fracture Faces	ff	Smooth and clean fractures	Polygenetic		V-Shaped Percussion Cracks	vc	V-shaped fractures or indentations with typical sizes ranging from 1 μm to 30 μm	Percussion	

FIG. 3A.—Photos and description of microtextures used in this study. Scale bars are 100  $\mu\text{m}$  unless otherwise noted. The symbol  $\mu\text{m}$  is written as  $\mu\text{m}$ .

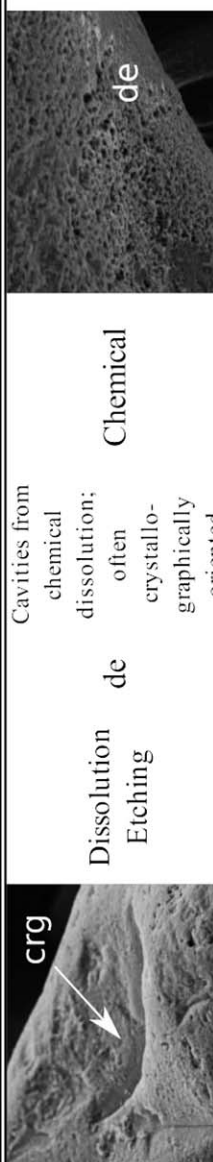
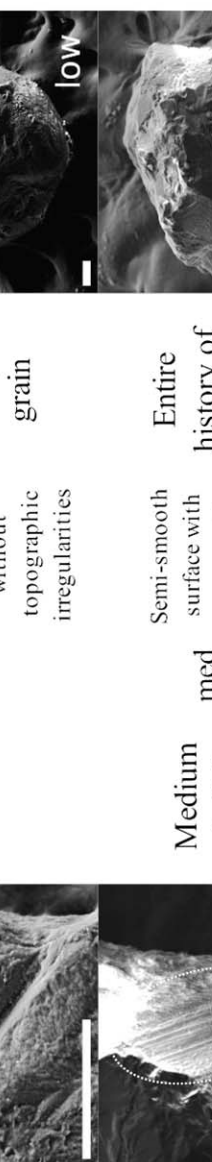
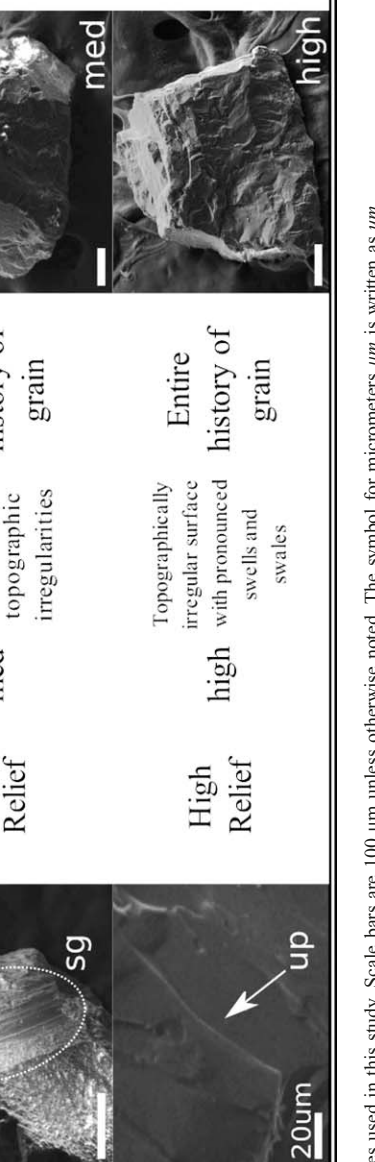
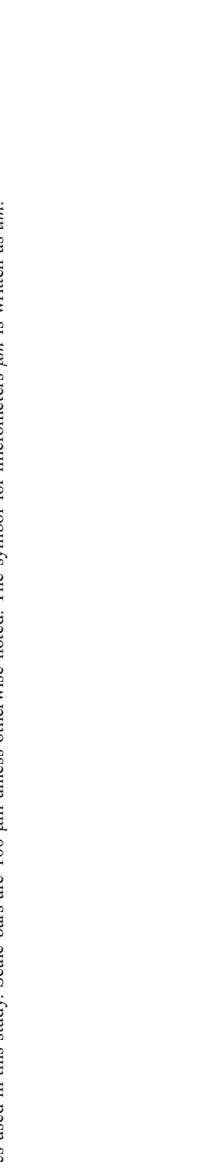
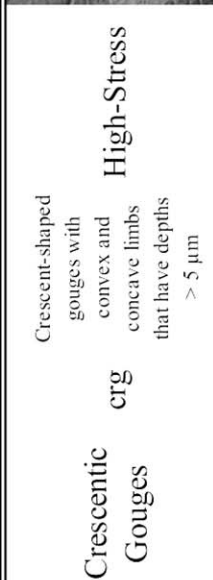
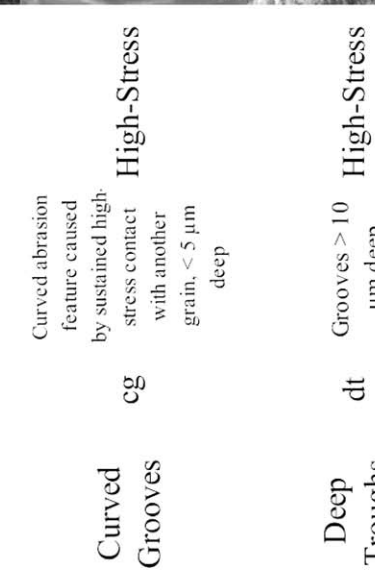
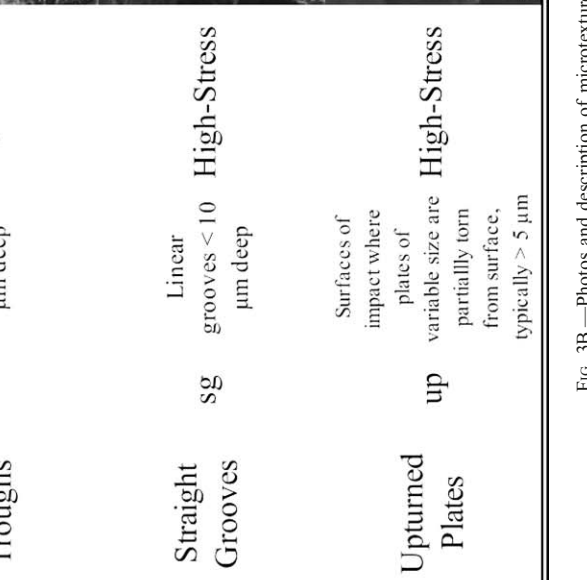
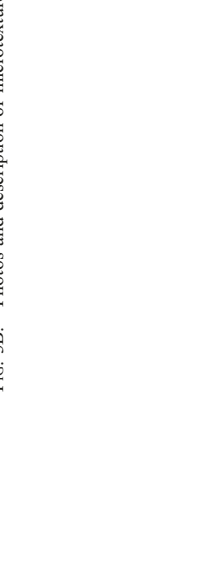
Microtexture	Abbr.	Description	Formation Process	Example Photo	Microtexture	Abbr.	Description	Formation Process	Example Photo
Crescentic Gouges	erg	Crescent-shaped gouges with convex and concave limbs that have depths $> 5 \mu\text{m}$	High-Stress		crg	Dissolution Etching	de	Cavities from chemical dissolution; often crystallographically oriented	
Curved Grooves	cg	Curved abrasion feature caused by sustained high-stress contact with another grain, $< 5 \mu\text{m}$ deep	High-Stress		cg	Precipitation Features	pf	Coatings of amorphous silica precipitation	
Deep Troughs	dt	Grooves $> 10 \mu\text{m}$ deep	High-Stress		dt	Low Relief	low	Nearly smooth surface without topographic irregularities	
Straight Grooves	sg	Linear grooves $< 10 \mu\text{m}$ deep	High-Stress		sg	Medium Relief	med	Semi-smooth surface with topographic irregularities	
Upturned Plates	up	Surfaces of impact where plates of variable size are partially torn from surface, typically $> 5 \mu\text{m}$	High-Stress		up	High Relief	high	Topographically irregular surface with pronounced swells and swales	

FIG. 3B.—Photos and description of microtextures used in this study. Scale bars are 100  $\mu\text{m}$  unless otherwise noted. The symbol for micrometers  $\mu\text{m}$  is written as  $\mu\text{m}$ .

### Principal-Component Analysis (PCA)

We performed PCA on the modern and ancient suites of microtextural data using Scikit-learn 0.21.2 (Pedregosa et al. 2011). This ordination excluded microtextures that were not analyzed by all authors, leaving 12 microtextures that were analyzed by every author in the dataset. These microtextures were arc-shaped steps, conchoidal fractures, linear steps, sharp angular features, subparallel linear fractures, edge rounding, v-shaped percussion cracks, curved grooves, precipitated features, low relief, medium relief, and high relief (Fig. 3; Tables S1–S2).

The principal-component axes are first derived from the modern suite of microtextural data and then the ancient samples are fitted to these new axes. These axes are shown in three biplots: PC1 vs. PC2; PC1 vs. PC3; and PC2 vs. PC3. In each biplot, 95% confidence ellipses centered at the mean were calculated for each modern transport mode using the methods of Schelp (2019). The broken-stick criterion (Frontier 1976; Jackson 1993; Legendre and Legendre 1998; Peres-Neto et al. 2003) was used to determine the significance of the microtextural loadings.

## RESULTS

### Bråvika Member Field Observations

Field observations of the Bråvika Member in Buldrevågen ( $79^{\circ} 59' 29''$  N,  $17^{\circ} 31' 20''$  E), Geerabukta ( $79^{\circ} 38' 06''$  N,  $17^{\circ} 43' 48''$  E), and Gimleodden ( $79^{\circ} 48' 19''$  N,  $18^{\circ} 24' 04''$  E) show evidence of bedforms with 5–10 m wavelength and 1–3 m amplitude, trough cross-bedding, adhesion ripples, pinstripe lamination (at 9 m in Fig. 2C) and grains that are frosted, well rounded, and well sorted (Fig. 4A–G). At the Gimleodden site, there is also evidence of soft-sediment deformation in the Bråvika Member at the contact with the Wilsonbreen Formation (Fig. 4I). At the Buldrevågen site, the Bråvika Member hosts sandstone intraclasts with diffuse boundaries and no obvious cements at 22 m above the base of the Bråvika Member, as well as pebbly sandstone intraclast conglomerates at 18 m and 22 m (7 m and 3 m below the Wilsonbreen Formation contact, respectively; Figs. 2C, 4J, K). The pebbly sandstone intraclast conglomerate is similar in color to the overlying Wilsonbreen Formation (Fig. 4L).

### Microtextural Dataset Description

This microtextural dataset is composed of 113 data points from modern and ancient aeolian, fluvial, and glacial settings. Ninety-two of these data points come from modern settings and 21 come from ancient settings. The data are compiled from 10 studies: this study (10% of the total datapoints), Smith et al. (2018) (22%), Kalińska-Nartiša et al. (2017) (4%), Nartišs and Kalińska-Nartiša (2017) (2%), Sweet and Brannan (2016) (35%), Stevic (2015) (2%), Deane (2010) (8%), Mahaney et al. (2001) (3%), Mahaney et al. (1996) (10%), and Mahaney and Kalm (1995) (4%). Most data points in this analysis represent a single sample of  $N$  grains. The data points from Mahaney and Kalm (1995) and Mahaney et al. (2001) are instead the published averages of larger sets of unavailable raw data from each study.

In the modern samples, 10% of the samples are aeolian, 45% are fluvial, and 45% are glacial. 60% of the modern aeolian samples come from periglacial settings, and 73% of the modern fluvial samples come from glaciofluvial settings. All of the modern glacial samples come from active glacial environments. In the ancient samples, 90% are constrained to particular depositional environments: 10% of the samples are aeolian, 10% are fluvial, and 71% are glacial. The remaining 10% of the ancient samples are from the Cryogenian Bråvika Member, and determining their depositional setting is a goal of this study.

### Probability of Occurrence

**Modern Samples.**—Modern aeolian samples are the most likely to have edge rounding (0.90 avg.), precipitated features (0.59 avg.), and low

relief (0.31 avg.) compared to modern fluvial and glacial samples, which in turn are more likely to have high relief (0.40 fluvial avg.; 0.36 glacial avg.) and subparallel linear fractures (0.63 fluvial avg.; 0.50 glacial avg.) (Fig. 5). These transport modes also share similar probabilities of occurrence for some features. Glacial and aeolian samples share similar probabilities of curved grooves (0.33 glacial avg., 0.27 aeolian avg.) compared to fluvial samples. Fluvial and aeolian samples also share similar probabilities of v-shaped percussion cracks (0.45 fluvial avg., 0.48 aeolian avg.) compared to glacial samples. The probability of occurrence of arc-shaped steps, conchoidal fractures, linear steps, sharp angular features, and medium relief are not substantially different between the three transport modes.

Study-specific variations in microtextural probabilities occur in each transport mode. In the aeolian transport mode, samples from Stevic (2015) (samples 20, 21; Table 1) are more likely to have curved grooves (0.80–0.93) compared with other aeolian samples in the dataset (0.13–0.19). The fluvial grains from Sweet and Brannan (2016) (sample 19) are more likely to have v-shaped percussion cracks (0.82) compared with the remaining fluvial samples from Smith et al. (2018) (0.15–0.40). Glacial grains from this study (samples 6–9) and Kalińska-Nartiša et al. (2017) (sample 17) have the highest probabilities of edge rounding (0.29–0.91) and precipitated features (0.55–0.88) compared with the remaining glacial samples. The glacial grains from Kalińska-Nartiša et al. (2017) are also the most likely to have low relief (0.68).

**Ancient Samples.**—Both samples from the Cryogenian Bråvika Member (samples 32, 33; Table 2) have high probabilities of edge rounding (1.00), precipitated features (1.00), and upturned plates (0.85–0.97; Fig. 6). Pleistocene aeolian sand samples from Nartišs and Kalińska-Nartiša (2017) (samples 34, 35) have high abundances of edge rounding, dissolution etching, and precipitated features (all categorized as “abundant”; > 0.75 probability of occurrence). Grains from the middle Devonian Arküla Stage fluvial sand samples (sample 45) and Pleistocene glaciofluvial sand samples (sample 46) from Estonia (Mahaney et al. 2001) are more likely to have edge rounding (0.56–0.64), v-shaped percussion cracks (0.53–0.61), and low relief (0.35–0.59) compared with grains from the modern fluvial average. The fluvial samples from Mahaney et al. (2001) also have lower probabilities of arc-shaped steps (0.00–0.23), conchoidal fractures (0.06–0.39), linear steps (0.00–0.26), subparallel linear fractures (0.08–0.35), upturned plates (0.00–0.04), and high relief (0.05–0.18) compared with the modern fluvial average. Grains from the Pleistocene tills in Costa Rica and the Dominican Republic (samples 36–44; Deane 2010) are more likely to have subparallel linear fractures (0.86–0.96) and medium relief (0.60–0.76) compared with the modern glacial average. The Pleistocene tills from Mahaney et al. (2001) (sample 47) and Mahaney and Kalm (1995) (samples 48–52) are broadly comparable to the modern glacial average.

### Principal-Component Analysis

In the PCA ordination, the PC1, PC2, and PC3 axes capture about 66% of the variance in the modern dataset (27.01%, 21.33%, and 17.43%, respectively). Along the PC1 axis (Figs. 7, 8; Table S3), the aeolian, fluvial, and glacial samples are distributed along both sides of the axis with no clear separation. However, the samples are generally separated by study along PC1: the samples from Stevic (2015) and Smith et al. (2018) are distributed between –2.9 and –1.1 and the samples from Mahaney et al. (1996) and Sweet and Brannan (2016) are distributed between –0.2 and 3.5. The samples from this study and Kalińska-Nartiša et al. (2017) are widely distributed on PC1, where the samples from this study are distributed between –3.2 to 3.3 and the Kalińska-Nartiša et al. (2017) samples are distributed between –3.1 and 1.7. The sample separation along PC1 is predominantly driven by the abundance of linear steps and arc-shaped steps, which have the largest (–0.489) and second largest (–0.425)

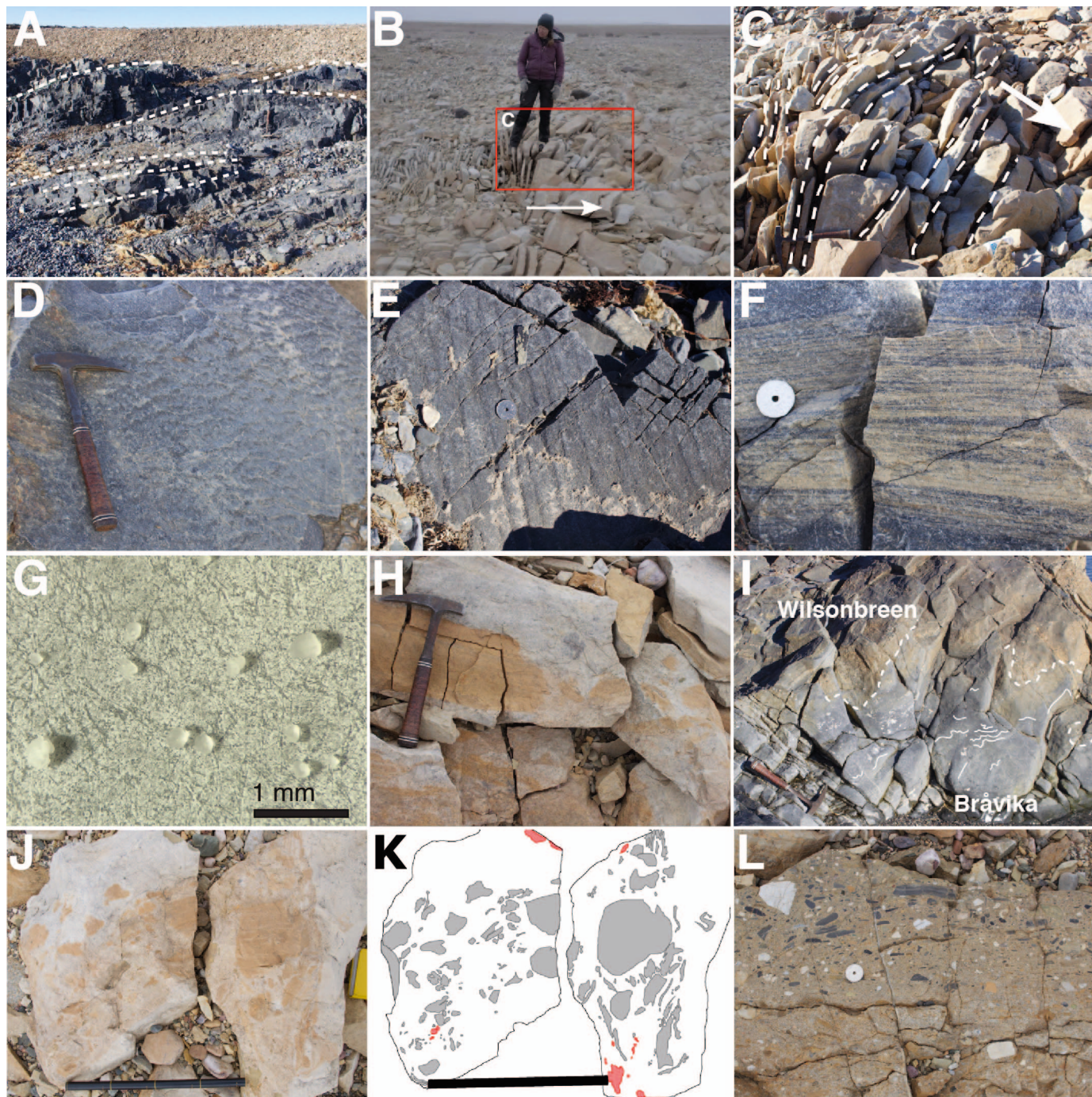


FIG. 4.—Field observations of the Bråvika Member and related units. All field photographs are of the Bråvika Member and are credited to K.D. Bergmann unless otherwise noted. **A**) Annotated photograph of large-scale bedforms exposed at Gimleodden. Dashed lines trace bedding surfaces. Hammer for scale. **B**) Photograph of frost-shattered trough crossbedding at 12 m in Buldrevågen (Fig. 2C), where the fracture planes are bedding surfaces. Arrow points upsection. The box highlights the location of Part C) (Photo credit: A.B. Jost). **C**) Annotated close-up of trough crossbedding. The dashed lines trace bedding surfaces and the arrow points upsection. **D**) Adhesion ripples on a bedding plane at Geerabukta. **E**) Potential adhesion ripples on a bedding plane at Gimleodden. **F**) Pinstripe lamination at Geerabukta. **G**) Photomicrograph of frosted grains from the Bråvika Member at Buldrevågen after dissolution of the dolomite cement with acid (Photo credit: J.N. Reahl). **H**) Close-up of sand intraclasts with diffuse edges at Buldrevågen (photo credit: T.J. Mackey). **I**) Soft-sediment deformation in the upper Bråvika Member under the Wilsonbreen tillite at Gimleodden, consistent with deformation of un lithified Bråvika sand by overriding ice. Dashed line marks the diffuse contact between the two units and solid lines trace contorted, folded beds in the Bråvika Member. Hammer for scale. **J**) Sandstone intraclasts with diffuse boundaries and greenish tan, pebbly, coarse sandstone intraclasts at 22 m in Buldrevågen (Fig. 2C). Bar is 40 cm long. **K**) Line drawing of Part J at the same scale; sandstone intraclasts are shaded gray, and greenish tan pebbly, coarse sandstone intraclasts are shaded red. **L**) The Wilsonbreen Formation at Buldrevågen, pictured here, has a greenish tan pebbly sandstone matrix.

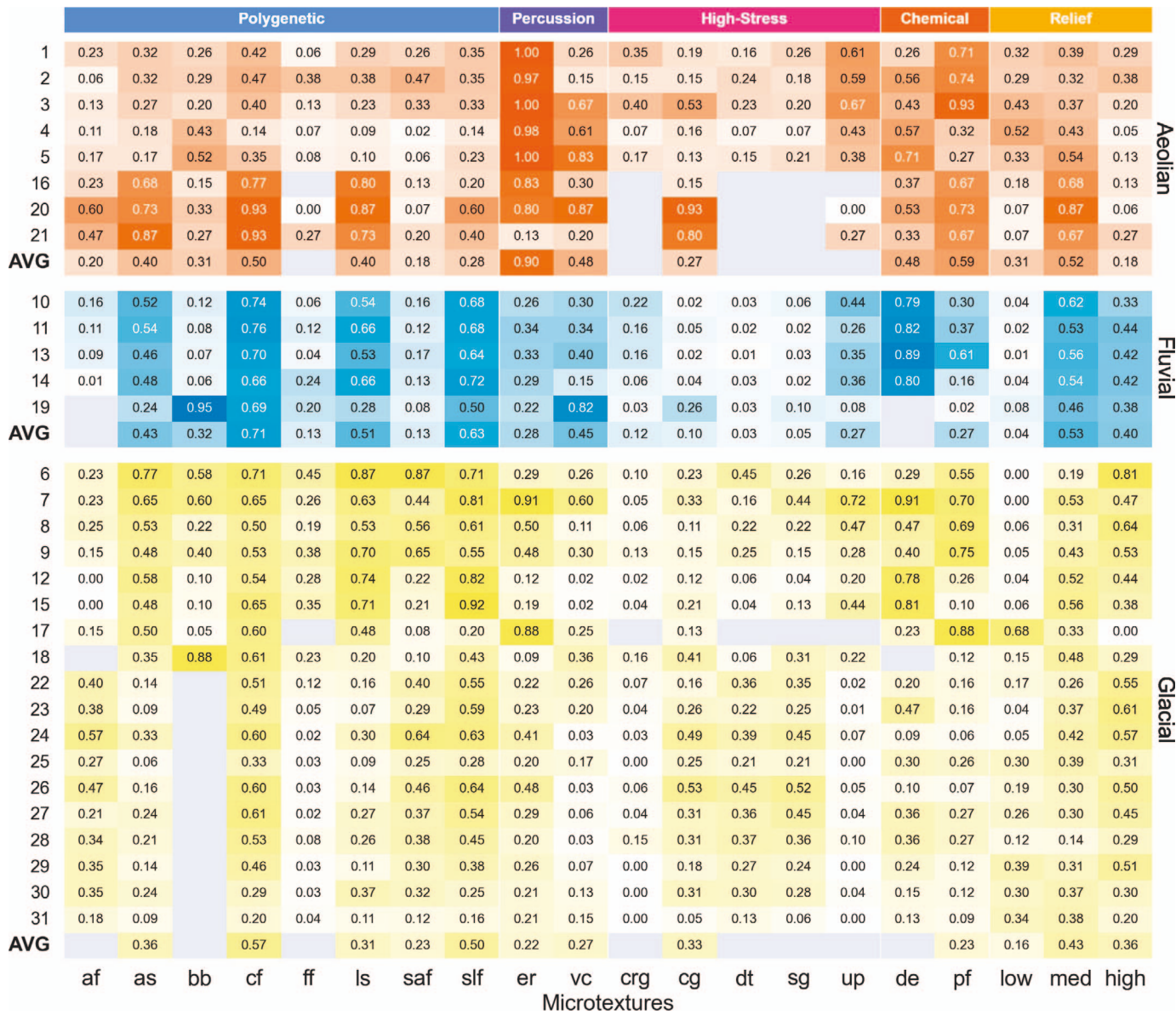


Fig. 5.—Heatmap of the microtextural probabilities of occurrence from 0 to 1 for each modern sample group used in the analysis. Samples are binned into aeolian, fluvial, and glacial transport modes. Refer to Table 1 for sample group numbers and descriptions. Data are averaged for sample groups that contain more than one sample ( $S > 1$ ). Refer to Figure 3A and B for microtextural abbreviations. The average of each transport mode for the modern samples (AVG) is at the bottom of each bin. Microtextures that were not analyzed in a study are grayed out.

negative loadings along PC1 (Table 3). However, neither of these loadings are strongly associated with PC1 according to the broken-stick criterion.

Along the PC2 axis, modern aeolian samples are distinctly separated from modern glacial and fluvial samples. This separation between aeolian and fluvial/glacial samples along PC2 is driven by low relief, edge rounding, and precipitated features in the positive direction (loadings of 0.457, 0.455, and 0.432) and high relief in the negative direction (-0.427), of which are all associated with PC2 according to the broken-stick criterion.

Along the PC3 axis, the three transport modes are distributed along both sides of the axis with no clear separation, similar to the distribution along PC1. However, unlike the distribution along PC1, the samples are not as distinctly separated by study. The significant microtextures along PC3 are sharp angular features and high relief in the positive direction (0.592 and 0.411), and medium relief in the negative direction (-0.482). All of these

microtextures are associated with PC3 according to the broken-stick criterion.

Along each principal-component axis, at least 89% of the ancient aeolian, fluvial, and glacial samples plot within the upper and lower adjacent values of the boxplot of their modern counterparts: 89% on PC1, 95% on PC2, and 100% on PC3 (Fig. 7). In each biplot (Fig. 8), at least 74% of these ancient samples plot within the 95% confidence ellipses of their modern counterparts: 89% in the PC1-PC2 biplot (A3), 74% in the PC1-PC3 biplot (B3), and 95% in the PC2-PC3 biplot (C3). The median of the percent agreement between the ancient samples and their modern counterparts is 92%.

The 92% median agreement between the modern and ancient samples demonstrates that PCA of modern and ancient samples provides a valid framework for interpreting the fingerprint of depositional environments in ancient samples with ambiguous depositional histories. In this ordination,

	Polygenetic								Percussion		High-Stress				Chemical		Relief			
32	0.21	0.08	0.46	0.38	0.13	0.21	0.18	0.18	1.00	1.00	0.05	0.15	0.23	0.13	0.97	0.49	1.00	0.64	0.33	0.03
33	0.03	0.20	0.65	0.40	0.03	0.20	0.45	0.13	1.00	0.70	0.03	0.15	0.03	0.08	0.85	0.90	1.00	0.55	0.30	0.15
34	0.06	0.06		0.00		0.06	0.00	0.00	0.75	0.06		0.06			0.06	0.75	0.75	0.00	0.50	0.06
35	0.06	0.06		0.06		0.06	0.00	0.00	0.75	0.06		0.06			0.06	0.75	0.75	0.50	0.06	0.00
<b>M. AVG</b>	<b>0.20</b>	<b>0.40</b>	<b>0.31</b>	<b>0.50</b>		<b>0.40</b>	<b>0.18</b>	<b>0.28</b>	<b>0.90</b>	<b>0.48</b>		<b>0.27</b>				<b>0.48</b>	<b>0.59</b>	<b>0.31</b>	<b>0.52</b>	<b>0.18</b>
45	0.54	0.00		0.06	0.02	0.00	0.00	0.08	0.64	0.61	0.00	0.00	0.00	0.00	0.45	0.45	0.59	0.39	0.08	Fluvial
46	0.40	0.00		0.18	0.00	0.00	0.02	0.21	0.56	0.53	0.00	0.00	0.00	0.00	0.14	0.03	0.35	0.42	0.18	
<b>M. AVG</b>		<b>0.43</b>	<b>0.32</b>	<b>0.71</b>	<b>0.13</b>	<b>0.51</b>	<b>0.13</b>	<b>0.63</b>	<b>0.28</b>	<b>0.45</b>	<b>0.12</b>	<b>0.10</b>	<b>0.03</b>	<b>0.05</b>	<b>0.27</b>		<b>0.27</b>	<b>0.04</b>	<b>0.53</b>	<b>0.40</b>
36	0.36	0.11	0.16	0.55	0.08	0.14	0.44	0.86	0.02	0.20	0.10	0.22	0.12	0.35	0.26	0.75	0.45	0.06	0.60	0.34
37	0.23	0.04	0.05	0.61	0.00	0.09	0.18	0.94	0.05	0.06	0.07	0.18	0.14	0.19	0.28	0.64	0.46	0.08	0.72	0.20
38	0.43	0.16	0.10	0.59	0.08	0.17	0.58	0.95	0.04	0.29	0.07	0.40	0.14	0.30	0.29	0.67	0.59	0.05	0.64	0.31
39	0.31	0.12	0.03	0.72	0.02	0.16	0.23	0.96	0.10	0.14	0.06	0.15	0.13	0.23	0.33	0.74	0.49	0.03	0.70	0.27
40	0.44	0.02	0.06	0.58	0.08	0.07	0.34	0.87	0.03	0.10	0.05	0.17	0.14	0.28	0.24	0.71	0.41	0.07	0.73	0.20
41	0.24	0.05	0.10	0.61	0.03	0.10	0.28	0.94	0.00	0.01	0.04	0.25	0.07	0.22	0.28	0.61	0.31	0.11	0.68	0.21
42	0.22	0.03	0.10	0.75	0.04	0.11	0.09	0.98	0.01	0.06	0.03	0.15	0.04	0.17	0.54	0.73	0.35	0.02	0.73	0.25
43	0.18	0.05	0.17	0.71	0.01	0.15	0.23	0.99	0.00	0.12	0.03	0.17	0.08	0.18	0.34	0.61	0.28	0.05	0.76	0.19
44	0.46	0.13	0.24	0.62	0.11	0.11	0.39	0.94	0.03	0.11	0.11	0.41	0.17	0.36	0.34	0.62	0.47	0.11	0.66	0.23
47	0.46	0.02		0.51	0.02	0.13	0.46	0.46	0.18	0.20	0.00	0.10	0.20	0.13	0.17	0.18	0.17	0.05	0.20	0.58
48	0.38	0.00		0.44	0.00	0.10	0.34	0.36	0.30	0.33	0.00	0.19	0.34	0.30	0.00	0.49	0.50	0.29	0.39	0.44
49	0.46	0.00		0.44	0.00	0.20	0.37	0.56	0.37	0.30	0.00	0.20	0.34	0.33	0.00	0.43	0.45	0.30	0.37	0.49
50	0.39	0.03		0.39	0.00	0.26	0.37	0.46	0.26	0.20	0.06	0.16	0.39	0.32	0.00	0.17	0.21	0.13	0.26	0.44
51	0.47	0.04		0.44	0.00	0.20	0.49	0.48	0.16	0.11	0.07	0.21	0.49	0.34	0.00	0.12	0.16	0.20	0.31	0.58
52	0.45	0.21		0.51	0.03	0.26	0.46	0.51	0.11	0.07	0.07	0.27	0.63	0.37	0.00	0.19	0.07	0.19	0.37	0.47
<b>M. AVG</b>		<b>0.36</b>		<b>0.57</b>		<b>0.31</b>	<b>0.23</b>	<b>0.50</b>	<b>0.22</b>	<b>0.27</b>		<b>0.33</b>					<b>0.23</b>	<b>0.16</b>	<b>0.43</b>	<b>0.36</b>
	af	as	bb	cf	ff	ls	saf	slf	er	vc	crg	cg	dt	sg	up	de	pf	low	med	high
	Microtextures																			

FIG. 6.—Heatmap of the microtextural probabilities of occurrence from 0 to 1 for each ancient sample group used in the analysis. Samples are binned into “unknown” (UNK; Bråvika Member), aeolian, fluvial, and glacial transport modes. Refer to Table 2 for sample group numbers and descriptions. Data are averaged for sample groups that contain more than one sample ( $S > 1$ ). Refer to Figure 3A and B for microtextural abbreviations. The average of each transport mode for the modern samples (M. AVG) from Figure 5 is at the bottom of each bin. Microtextures that were not analyzed in a study are grayed out.

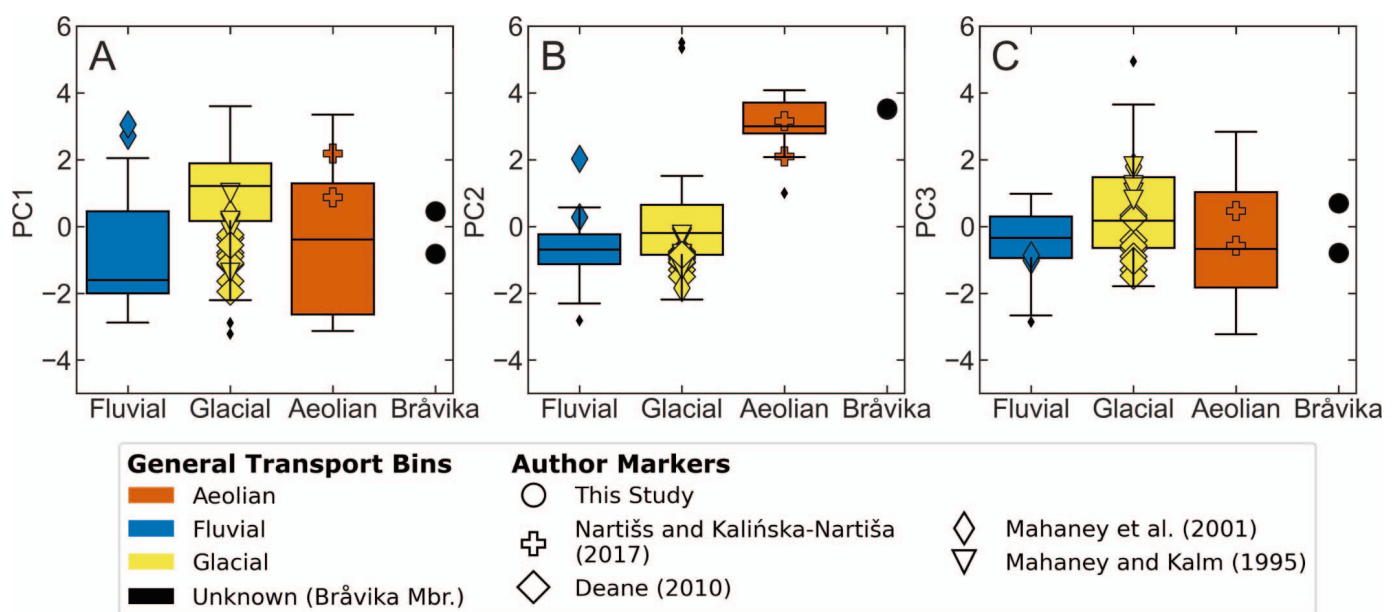


FIG. 7.—Boxplots of the modern aeolian, fluvial, and glacial samples along the A) PC1, B) PC2, and C) PC3 axes. The small black diamonds represent modern outliers for each transport mode. The ancient samples are plotted as individual points over the boxplots.

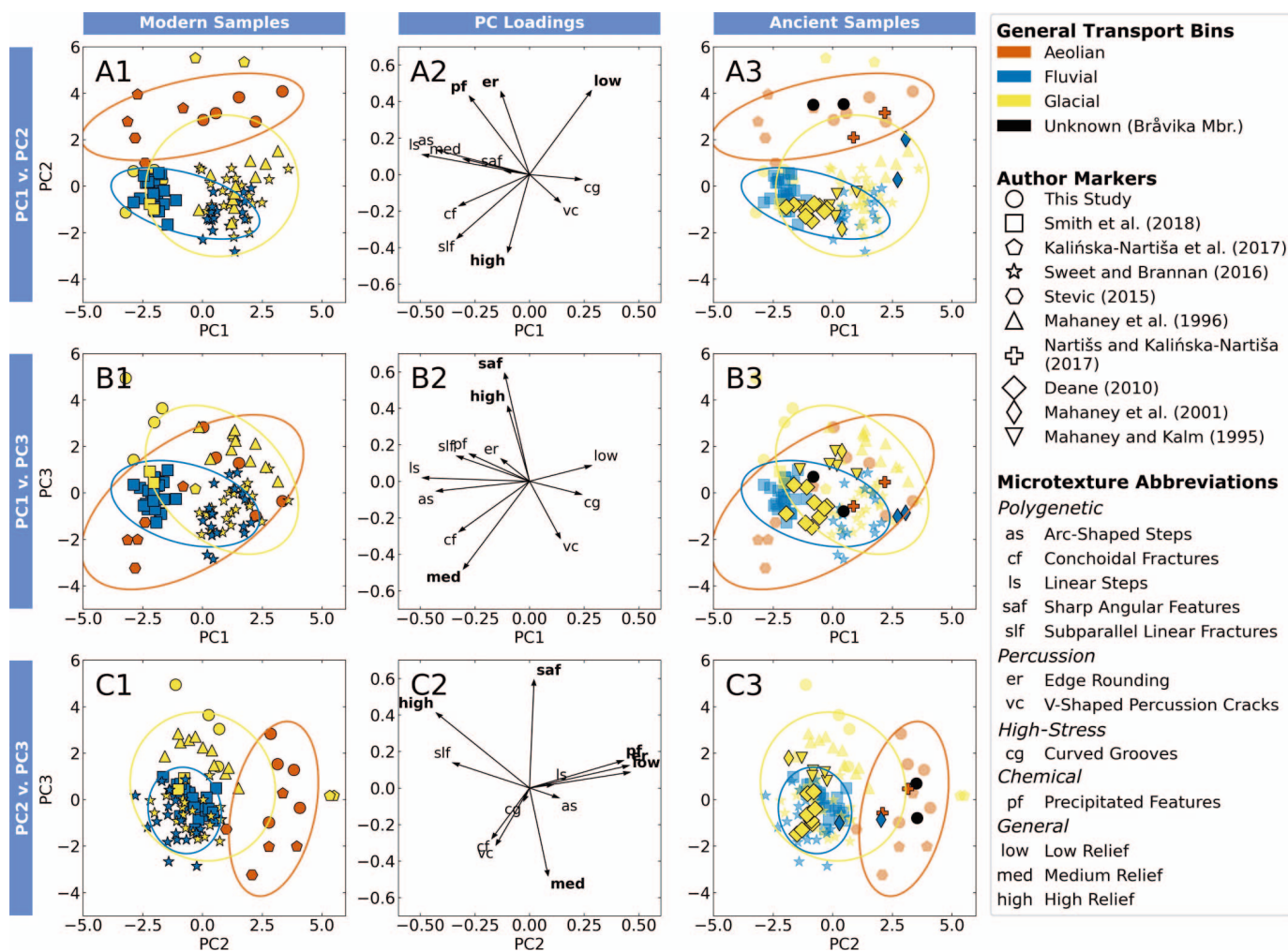


FIG. 8.—PCA ordination using all 12 microtextures analyzed by all studies. Each row is a biplot in A) PC1–PC2 space, B) PC1–PC3 space, and C) PC2–PC3 space. Column 1 plots the modern sample data in each space (this study through Mahaney et al. 1996), Column 2 plots the microtextural loadings, and Column 3 plots the ancient sample data (this study, Nartišs and Kalińska-Nartiša 2017 through Mahaney and Kalm 1995) over the existing modern reference frame. Refer to Table 3 for the loadings in Column 2. Microtextures with significant loadings in Column 2 are in bold. The ellipses are 95% confidence intervals of each modern transport mode that are centered at the mean of the transport mode in each coordinate space. The ellipses are calculated using the methods of Schelp (2019).

TABLE 3.—Ranked loadings and squared loadings of microtextures from the PCA ordination (Fig. 8). Refer to Figure 3A and B for microtexture abbreviations. The microtextures in bold have squared loadings that are greater than the expected value of their associated principal component according to the broken-stick criterion (Frontier 1976; Jackson 1993; Legendre and Legendre 1998; Peres-Neto et al. 2003).

PC1			PC2			PC3		
Expected PC Value:	0.259		Expected PC Value:	0.175		Expected PC Value:	0.134	
Microtexture	Loading	Loading <sup>2</sup>	Microtexture	Loading	Loading <sup>2</sup>	Microtexture	Loading	Loading <sup>2</sup>
low	0.286	0.082	low	<b>0.457</b>	<b>0.209</b>	saf	<b>0.592</b>	<b>0.351</b>
cg	0.239	0.057	er	<b>0.455</b>	<b>0.207</b>	high	<b>0.411</b>	<b>0.169</b>
vc	0.141	0.020	pf	<b>0.432</b>	<b>0.186</b>	pf	0.153	0.023
high	-0.104	0.011	as	0.139	0.019	slf	0.135	0.018
saf	-0.114	0.013	ls	0.112	0.013	er	0.126	0.016
er	-0.128	0.017	med	0.090	0.008	low	0.089	0.008
pf	-0.272	0.074	saf	0.018	0.000	ls	0.019	0.000
med	-0.300	0.090	cg	-0.028	0.001	as	-0.055	0.003
cf	-0.324	0.105	vc	-0.153	0.023	cg	-0.071	0.005
slf	-0.335	0.112	cf	-0.168	0.028	cf	-0.279	0.078
as	-0.425	0.181	slf	-0.350	0.123	vc	-0.312	0.097
ls	-0.489	0.239	high	<b>-0.427</b>	<b>0.182</b>	med	<b>-0.482</b>	<b>0.232</b>

the two Bråvika Member samples with ambiguous depositional histories consistently plot within the upper and lower adjacent values of the modern aeolian samples in each principal-component axis (Fig. 7) and the 95% confidence ellipses of the modern aeolian samples in each biplot (Fig. 8). This placement suggests that the Bråvika Member samples analyzed in this study have an aeolian origin.

## DISCUSSION

### *Interpreting the PCA Ordination*

PC1 separates the modern samples by author and accounts for the most variance in the dataset (27.01%), indicating that author-specific microtextural variance is the largest individual source of variance in the modern dataset. This result is consistent with the observation that SEM operator variance exerts significant influence on the probabilities of occurrence of individual microtextures (Culver et al. 1983). However, as Culver et al. (1983) observed using canonical variate analysis, author variance is overall negligible in determining a sample's depositional environment: the combined variance of PC2 and PC3 accounts for over a third of the variance in the modern dataset (21.33% and 17.43%, respectively). The PC2 axis separates the samples into aeolian transport modes and fluvial and glacial transport modes, and the PC3 axis separates the samples neither by transport mode nor by study (Fig. 8).

### *Which Microtextures Distinguish Transport Modes?*

Aeolian sediment is defined by high probabilities of low relief, edge rounding, and precipitated features, and fluvial and glacial sediments are defined by high probabilities of high relief and subparallel linear fractures. The modern (Fig. 5) and ancient (Fig. 6) heatmaps show that aeolian samples have the highest probabilities of low relief, edge rounding, and precipitated features, and fluvial and glacial samples have the highest probabilities of high relief and subparallel linear fractures. PC2 also separates the aeolian samples from the fluvial and glacial samples using low relief, edge rounding, and precipitated features in the positive (aeolian) direction and high relief in the negative (fluvial and glacial) direction (Fig. 8; Table 3). These findings are consistent with previous observations of these microtextures: low relief, edge rounding, and precipitated features have all previously been associated with windblown sediment (Nieter and Krinsley 1976; Lindé and Mycielska-Dowgiallo 1980; Krinsley and Trusty 1985; Mahaney 2002; Vos et al. 2014); high relief can occur on both fluvial and glacial sediments (Mahaney 2002; Vos et al. 2014); and subparallel linear fractures are often associated with glacial and glaciofluvial settings, the latter of which makes up 73% of the modern fluvial samples in this study (Mahaney and Kalm 2000; Deane 2010; Immonen 2013; Vos et al. 2014; Woronko 2016).

Although fluvial and glacial samples are microtexturally distinct from aeolian samples, it is difficult to disambiguate the fluvial and glacial transport modes from each other in this dataset. Features that are typically associated with glacial environments, such as arc-shaped steps, conchoidal fractures, linear steps, and sharp angular features (Mahaney and Kalm 2000; Mahaney 2002; Immonen 2013; Woronko 2016), had comparable probabilities across all three modern transport modes, indicating that these features are not exclusively associated with glacial environments (Fig. 5). Smith et al. (2018) also observed that arc-shaped steps and linear steps may not be indicators of glacial transport. These results are consistent with Sweet and Soreghan's (2010) classification of these features as *polygenetic* features that are formed through a variety of transport processes. Subparallel linear fractures are also associated with glacial and glaciofluvial settings (Mahaney and Kalm 2000; Deane 2010; Immonen 2013; Vos et al. 2014; Woronko 2016), but the modern fluvial average for subparallel linear fractures is higher than the glacial average. Although glaciofluvial samples make up 73% of the modern fluvial samples, the non-

glacial fluvial samples (samples 10 and 13; Fig. 5) have similar probabilities of subparallel linear fractures compared to glaciofluvial samples (samples 11, 14, and 19), suggesting that subparallel linear fractures may not be an exclusively glacial feature. These results suggest that fluvial and glacial samples may share microtextural similarities, but more studies comparing the microtextural features of non-glacial fluvial, glaciofluvial, and glacial samples are needed to understand the differences between these transport environments.

These results highlight the importance of precipitated features as a primary indicator of transport instead of an exclusive product of diagenesis. If precipitated features were only an indicator of postdepositional diagenesis, then the probability of precipitated features should increase with age. However, all of the modern samples have some probability of having precipitated features—particularly the aeolian samples—and the ancient samples do not show a consistent increase in the probability of chemical features as the sediment age increases (Figs. 5, 6). Both of these observations point to precipitated features being a primary microtextural feature. Although Sweet and Soreghan (2010) suggested that precipitated features should not be counted because they can form via diagenesis and overprint a sample, our results indicate that these features can also be a primary feature and should not be discounted, even in situations where diagenesis is a concern.

Some microtextures often used in microtextural studies could not be included in this analysis: abraded features, breakage blocks, crescentic gouges, fracture faces, deep troughs, straight grooves, upturned plates, and dissolution etching. Many of these microtextures have been previously associated with certain transport environments. Breakage blocks, straight grooves, and fracture faces have been associated with glacial environments (Woronko 2016), and upturned plates and dissolution etching have been associated with aeolian environments (Margolis and Krinsley 1974; Mahaney 2002). For the purposes of comparing microtextural data from multiple studies, we were limited to using the most often used microtextures in the literature. Moving forward, it would be helpful to establish a consistent minimum set of microtextures to be used in microtextural studies.

### *Test Case: The Cryogenian Bråvika Member*

We now shift our focus to using the microtextural data, PCA, and stratigraphic observations to constrain the depositional environment of the Cryogenian Bråvika Member from Buldrevågen, Svalbard. Our combined field observations and microtextural data suggest that the Bråvika Member includes aeolian deposition that may be time equivalent with the onset of the syn-glacial Marinoan Wilsonbreen Formation.

The microtextural evidence points to an aeolian origin for the Bråvika Member. Both samples from the Bråvika Member have particularly high occurrences of edge rounding, precipitated features, and low relief (samples 32 and 33; Fig. 6), all of which have been previously associated with aeolian transport (Nieter and Krinsley 1976; Lindé and Mycielska-Dowgiallo 1980; Krinsley and Trusty 1985; Mahaney 2002; Vos et al. 2014). The Bråvika Member samples also have high probabilities of upturned plates, which have been associated with grain frosting (Margolis and Krinsley 1971). Compared to the modern and ancient aeolian, fluvial, and glacial samples, the Bråvika Member samples are most similar to the aeolian samples, sharing similar probabilities of low relief, edge rounding, and precipitated features (Fig. 6). These samples also consistently plot within the upper and lower adjacent values (Fig. 7) and 95% confidence ellipse (Fig. 8) of the modern aeolian samples. Because the ancient aeolian, fluvial, and glacial samples are accurately matched with their modern counterparts 92% of the time when transformed into modern PCA space, the PCA ordination is able to accurately plot samples with ambiguous depositional histories alongside their most likely modern microtextural analogs.

An aeolian interpretation for the microtextural data is consistent with field observations made in 2017 of the Bråvika Member in Buldrevågen, Geerabukta, and Gimleodden (Fig. 4). Bedforms with 5–10 m wavelengths and 1–3 m amplitudes at the Gimleodden (Fig. 4A) and Buldrevågen (Fig. 4B, C) sites are consistent with aeolian dunes in scale and style (Wilson 1972; Pye and Tsoar 2009). There is also evidence of adhesion ripples on bedding planes at the Geerabukta (Fig. 4D) and Gimleodden (Fig. 4E) sites. Adhesion ripples are formed when dry, windblown sand is blown onto a wet surface, and these features have been previously observed on ancient aeolian deposits (Kocurek and Fielder 1982). The presence of pinstripe lamination at the Buldrevågen (Fig. 2C) and Geerabukta (Fig. 4F) sites are a strong indicator for aeolian deposition (Fryberger and Schenck 1988). The high degree of grain rounding at this interval (Fig. 4G) is also characteristic of grains transported by aeolian processes (Folk 1980); subaqueous transport does not typically produce such a high degree of grain rounding (Pettijohn 1957). The frosted grains in these samples (Fig. 4G) are also a strong indicator of aeolian transport (Pye and Tsoar 2009).

Field evidence also suggests that the aeolian strata of the Bråvika Member may be syndepositional with the Marinoan pan-glaciation as opposed to the Cryogenian interglacial. The pebbly sandstone intraclast conglomerates' proximity to the contact with—and similar color and texture as—the Wilsonbreen Formation (Figs. 2, 4) suggest that they are sourced from this unit. These intraclasts' occurrences at 7 m and 3 m below the Wilsonbreen Formation contact (Fig. 2C) suggest that the Bråvika Member in Buldrevågen was syndepositional with the Wilsonbreen Formation and the Marinoan pan-glaciation. The intraclasts with diffuse boundaries and no obvious cements at 22 m (Figs. 2, 4) are putative ice-cemented sand intraclasts. Ice-cemented intraclasts form when water in the pore space of unconsolidated sand freezes parts of sand into discrete clasts that can be transported and deformed into new orientations before the cementing ice melts. Sand intraclasts are routinely identified as ice-cemented in glaciogenic deposits (Browne and Naish 2003), and Runkel et al. (2010) has reported putative ice-cemented sand intraclasts preserved in rocks as old as the middle to late Cambrian. The putative ice-cemented intraclasts indicate that the Bråvika Member was at least unconsolidated during the Marinoan pan-glaciation, and the occurrence of possible Wilsonbreen intraclasts 3 m below the Wilsonbreen Formation contact (Fig. 2C) suggests that the upper Bråvika Member was syndepositional with the Marinoan glaciation. Evidence of soft-sediment deformation at the contact between the Bråvika Member and Wilsonbreen Formation at Gimleodden (Fig. 4I) is also consistent with the upper Bråvika Member being unconsolidated during the Marinoan glaciation.

Integrating microtextural and field observations, we suggest that the upper Bråvika Member includes aeolian deposition and may represent a syn-glacial aeolian sand sea, or erg, contemporaneous with the Marinoan glaciation. This setting is akin to previously identified Marinoan syn-glacial ergs in the Bakoye Formation of Mali (Deynoux et al. 1989) and the Whyalla Sandstone (Elatina glaciation) of South Australia (Williams 1998; Rose et al. 2013; Ewing et al. 2014). Hoffman and Li (2009) suggested that katabatic winds coming off of the Marinoan ice sheet are the primary transport mechanism for these syn-glacial ergs. The northward paleoflow direction of the Bråvika Member and the Bråvika Member's reciprocal thickness relationship with the Wilsonbreen Formation (Halverson et al. 2004) may reflect this transport mechanism, where a northward-advancing ice margin represented by the Wilsonbreen Formation drives the Bråvika Member to the north with katabatic winds coming off of the Marinoan ice sheet.

The microtextural samples analyzed in this study are specific to the interval in Buldrevågen that is proximal to the Wilsonbreen contact. Given the wide range of possible facies proposed by Halverson et al. (2004), Halverson (2011), Hoffman et al. (2012), and this study, the Bråvika Member may represent multiple depositional environments across

localities that capture a transition from the Cryogenian interglacial to the Marinoan pan-glaciation.

Important questions remain about the apportionment of time in the strata that record the Cryogenian interglacial in Svalbard. The absence of the pre-Marinoan Trezona negative  $\delta^{13}\text{C}$  excursion below the Wilsonbreen Formation has been used to suggest that the sedimentary package between the Petrovbrean Member and the Wilsonbreen Formation is top-truncated (Hoffman et al. 2012; Fairchild et al. 2016; Halverson et al. 2018). The locations of the hatal surfaces in the Bråvika Member remain ambiguous, and their locations are critical to understanding the apportionment of time in these units and in the interglacial. Our work suggests that the uppermost aeolian deposition in the Bråvika Member is continuous with the start of Wilsonbreen deposition, but there may be important hatal surfaces lower in the Bråvika Member.

## CONCLUSIONS

Quartz surface microtextures preserve the transport histories of modern and ancient sediment. However, because workers count microtextures differently for samples from the same depositional environment, the defining microtextures of certain transport modes are not well constrained. We used PCA to directly compare quantitative microtextural data from modern and ancient aeolian, fluvial, and glacial sediments across workers. Although differences between workers are the largest sources of variance in the dataset, the PCA ordination shows that aeolian samples are microtexturally distinct from fluvial and glacial samples across studies. Fluvial and glacial samples are difficult to disambiguate from each other in this dataset, indicating that more work needs to be done comparing fluvial, glaciogenic, and glacial samples with each other. The PCA ordination also demonstrates that ancient sediments and modern sediments have quantitatively similar microtextural relationships. Therefore, PCA may be a useful tool to elucidate the ambiguous transport histories of some ancient sediment grains. As a test case, we used PCA to constrain the depositional environment of the ambiguous Cryogenian Bråvika Member from Svalbard. This ordination, combined with field observations, indicates that the Bråvika Member includes aeolian deposition, and suggests that the Bråvika Member may be analogous to syn-glacial Marinoan aeolian sand seas such as the Bakoye Formation in Mali and the Whyalla Sandstone in South Australia. This study demonstrates that PCA can distinguish sedimentary environments across multiple studies, which in turn helps constrain the depositional history of ambiguous sedimentary deposits like the Bråvika Member.

## SUPPLEMENTAL MATERIAL

All supplementary materials related to this study—including detailed sample descriptions, additional notes on PCA analysis, code, raw microtextural data, and SEM images—are available at [https://github.com/jreahl/Reahl\\_2020](https://github.com/jreahl/Reahl_2020) and from the SEPM Data Archive: <https://www.sepm.org/supplemental-materials>.

## LAND ACKNOWLEDGEMENT

This work, from analysis to writing, was performed at institutions built on Indigenous land, using samples collected from Indigenous lands. The samples analyzed for the first time in this study were collected from the traditional and ancestral territories of the Cocopah (*Kwapa*), Comanche (*Nt̄em̄n̄ut̄ut̄*), Keechi (*Ki:che:ss*), Kiowa (*ʃGáuiʃdóñ:gyá*), Kumeyaay, Osage (*Wahzhazhe*), Quechan (*Kwatsáam*), Salt River O'odham (Pima) and Piipaash (Maricopa), Taku River Tlingit (*Lingít*), Tawakoni (*Tawá:kharih*), Waco (*Wí:ko?*), and Wichita (*Kirikir?i:s*). Laboratory analysis and SEM analysis was performed on unceded Wampanoag land. Writing was performed on the territories of the Abenaki, Chumash, and Wampanoag. These communities occupied these territories before and after European colonization and live on this land to the present day. We also acknowledge the dispossession of Indigenous land through the 1862 Morrill Act,

which turned parcels of land taken from tribal nations into seed money for land-grant universities including the Massachusetts Institute of Technology. Although this acknowledgement does not compensate for centuries of injustices, we hope it helps spur robust, mutually beneficial collaboration between Indigenous communities and scientific efforts. We encourage readers to engage with Indigenous communities and cultures around where they live and work. The Native Land Digital database ([native-land.ca](http://native-land.ca)) is an excellent resource to begin this process. The best resources for prolonged learning are through direct conversation and collaboration with Indigenous community members. Many Indigenous communities have dedicated cultural heritage officers who may be available as partners in these efforts; the National Congress of American Indians ([ncai.org](http://ncai.org)) hosts a tribal directory with contact information, as well as the National Association of Tribal Historic Preservation Officers ([nathpo.org](http://nathpo.org)).

#### ACKNOWLEDGEMENTS

We thank the Salt River Pima–Maricopa Indian Community Cultural Resource Department, Justin Brundin (Cultural Resources Manager, Cocopah Indian Tribe), Andrea A. Hunter (Tribal Historic Preservation Officer, Osage Nation), Gary McAdams (Cultural Planner, Wichita and Affiliated Tribes), and Benjamin Louter (Heritage Coordinator, Taku River Tlingit First Nation) for assistance with acknowledging Indigenous territory. Adam B. Jost (Massachusetts Institute of Technology, MIT) performed field work in Svalbard with M.D.C., J.W., T.J.M., and K.D.B., collected photographs, and trained and assisted J.N.R. in the laboratory. We thank Steven M. Adams and Gerilyn S. Soreghan (University of Oklahoma) for collecting and providing samples from the Algodones Dunes and the Waynoka Dunes. The Juneau Icefield Research Program (JIRP), Foundation for Glacier and Environmental Research (FGER), and Coastal Helicopters in Juneau, Alaska provided logistical support, food, and lodging on the Juneau Icefield. This work began as J.N.R.’s undergraduate thesis project at Wellesley College. We thank Daniel J. Brabander, Katrin Monecke, and Wesley A. Watters at Wellesley College for being on the thesis committee. We thank Timothy J. Cavanaugh at the Harvard University Center for Nanoscale Systems (CNS) for assistance operating the SEM. The Harvard CNS is a member of the National Nanotechnology Coordinated Infrastructure Network (NNCI), which is supported by the National Science Foundation (NSF) under NSF award no. 1541959. K.D.B. acknowledges support from the Victor P. Starr Development Chair and the David and Lucille Packard Foundation. M.D.C. received support from a National Defense Science and Engineering Graduate Fellowship. J.W. received support from the Dean of the School of Science Fellowship at MIT. T.J.M. received support from the Agouron Geobiology Institute. Field work in Svalbard was supported by the MIT Wade Fund awarded to K.D.B. Samples from Antarctic lakes were collected during field work in the McMurdo Dry Valleys supported by NASA Astrobiology’s Exobiology and Evolutionary Biology Program (award no. NNX08AO19G); the New Zealand Foundation for Research, Science, and Technology (award no. C01X0306); and the NSF Division of Polar Programs’ McMurdo Long Term Ecological Research Project (award no. 1115245). Field work on the Juneau Icefield was partially funded by the National Association of Geoscience Teachers (NAGT) Scholarship for Field Study awarded to J.N.R. Thoughtful feedback from Pedro J.M. Costa and an anonymous reviewer improved the manuscript.

#### AUTHOR CONTRIBUTIONS

J.N.R. wrote the manuscript, collected samples from the Juneau Icefield, performed SEM analysis on all samples, and performed the PCA analysis. M.D.C. and K.D.B. were the primary advisors to J.N.R. J.W. shared her stratigraphic columns and samples of the Bråvika Member, as well as insight on statistics and machine learning. J.W., M.D.C., T.J.M., and K.D.B. characterized and collected samples of the Bråvika Member in Svalbard during their 2017 field season. T.J.M. contributed samples from the McMurdo Dry Valleys. All authors reviewed the final manuscript.

#### REFERENCES

ADAMS, S.M., 2018, Evaluating desert silt production using field, experimental, and remote-sensing methods [MS Thesis]: University of Oklahoma, 74 p.

ADAMS, S.M., AND SOREGHAN, G.S., 2020, A test of the efficacy of sand saltation for silt production: implications for the interpretation of loess: *Geology*, v. 48, p. 1105–1109.

BLACKWELDER, P.L., AND PILKEY, O.H., 1972, Electron microscopy of quartz grain surface textures: the U.S. Eastern Atlantic continental margin: *Journal of Sedimentary Petrology*, v. 42, p. 520–526.

BROWNE, G.H., AND NAISH, T.R., 2003, Facies development and sequence architecture of a late Quaternary fluvial–marine transition, Canterbury Plains and shelf, New Zealand: implications for forced regressive deposits: *Sedimentary Geology*, v. 158, p. 57–86.

BULL, P.A., 1981, Environmental reconstruction by electron microscopy: *Progress in Physical Geography*, v. 5, p. 368–397.

CALVER, C.R., CROWLEY, J.L., WINGATE, M.T.D., EVANS, D.A.D., RAUB, T.D., AND SCHMITZ, M.D., 2013, Globally synchronous Marinoan deglaciation indicated by U-Pb geochronology of the Cottons Breccia, Tasmania, Australia: *Geology*, v. 41, p. 1127–1130.

COCH, N.K., AND KRINSLEY, D.H., 1971, Comparison of stratigraphic and electron microscopic studies in Virginia Pleistocene coastal sediments: *The Journal of Geology*, v. 79, p. 426–437.

CONDON, D., ZHU, M., BOWRING, S., WANG, W., YANG, A., AND JIN, Y., 2005, U-Pb Ages from the Neoproterozoic Doushantuo Formation, China: *Science*, v. 308, p. 95–98.

COSTA, P.J.M., ANDRADE, C., DAWSON, A.G., MAHANEY, W.C., FREITAS, M.C., PARIS, R., AND TABORDA, R., 2012, Microtextural characteristics of quartz grains transported and deposited by tsunamis and storms: *Sedimentary Geology*, v. 275–276, p. 55–69.

COSTA, P.J.M., ANDRADE, C., MAHANEY, W.C., MARQUES DA SILVA, F., FREIRE, P., FREITAS, M.C., JANARDO, C., OLIVEIRA, M.A., SILVA, T., AND LOPES, V., 2013, Aeolian microtextures in silica spheres induced in a wind tunnel experiment: comparison with aeolian quartz: *Geomorphology*, v. 180–181, p. 120–129.

COSTA, P.J.M., PARK, Y.S., KIM, Y.D., QUINTELA, M., MAHANEY, W.C., DOURADO, F., AND DAWSON, S., 2017, Imprints in silica grains induced during an open-channel flow experiment: determination of microtextural signatures during aqueous transport: *Journal of Sedimentary Research*, v. 87, p. 677–687.

CULVER, S.J., BULL, P.A., CAMPBELL, S., SHAKESBY, R.A., AND WHALLEY, W.B., 1983, Environmental discrimination based on quartz grain surface textures: a statistical investigation: *Sedimentology*, v. 30, p. 129–136.

DEANE, S.M., 2010, Quartz grain microtextures and sediment provenance: using scanning electron microscopy to characterize tropical highland sediments from Costa Rica and the Dominican Republic [MS Thesis]: University of Tennessee, Knoxville, 137 p.

DEYNOUX, M., KOCUREK, G., AND PROUST, J.N., 1989, Late Proterozoic periglacial aeolian deposits on the West African Platform, Taoudeni Basin, western Mali: *Sedimentology*, v. 36, p. 531–549.

EWING, R.C., EISENMAN, I., LAMB, M.P., POPICK, L., MALOOF, A.C., AND FISCHER, W.W., 2014, New constraints on equatorial temperatures during a Late Neoproterozoic snowball Earth glaciation: *Earth and Planetary Science Letters*, v. 406, p. 110–122.

FAIRCHILD, I.J., FLEMING, E.J., BAO, H., BENN, D.I., BOOMER, I., DUBLYANSKY, Y.V., HALVERSON, G.P., HAMBREY, M.J., HENDY, C., McMILLAN, E.A., SPÖTL, C., STEVENSON, C.T.E., AND WYNN, P.M., 2016, Continental carbonate facies of a Neoproterozoic panglaciation, north-east Svalbard: *Sedimentology*, v. 63, p. 443–497.

FOLK, R.L., 1980, *Petrology of Sedimentary Rocks*: Austin, Texas, Hemphill Publishing, 190 p.

FRONTIER, S., 1976, Étude de la décroissance des valeurs propres dans une analyse en composantes principales: comparaison avec le modèle du bâton brisé: *Journal of Experimental Marine Biology*, v. 25, p. 67–75.

FRYBERGER, S.G., AND SCHENK, C.J., 1988, Pin stripe lamination: a distinctive feature of modern and ancient eolian sediments: *Sedimentary Geology*, v. 55, p. 1–15.

GOLDSTEIN, J.I., NEWBURY, D.E., ECHLIN, P., JOY, D.C., ROMIG, A.D., JR., LYMAN, C.D., FIORI, C., AND LIFSHIN, E., 1992, *Scanning Electron Microscopy and X-Ray Microanalysis*: Springer, 550 p.

GREEN, W.J., STAGE, B.R., BRATINA, B.J., WAGERS, S., PRESTON, A., O’BRYAN, K., SHACAT, J., AND NEWELL, S., 2004, Nickel, copper, zinc and cadmium cycling with manganese in Lake Vanda (Wright Valley, Antarctica): *Aquatic Geochemistry*, v. 10, p. 303–323.

GUMBLEY, J.W., 1975, A sedimentological study of three saline lakes in the Dry Valleys of Victoria Land, Antarctica [MS Thesis]: University of Waikato, 165 p.

HALVERSON, G.P., 2011, Glacial sediments and associated strata of the Polarisbreen Group, northeastern Svalbard, in Arnaud, E., Halverson, G.P., and Shields-Zhou, G., eds., *The Geological Record of Neoproterozoic Glaciations*: Geological Society of London, Memoirs, v. 36, p. 571–579.

HALVERSON, G.P., MALOOF, A.C., AND HOFFMAN, P.F., 2004, The Marinoan glaciation (Neoproterozoic) in northeast Svalbard: *Basin Research*, v. 16, p. 297–324.

HALVERSON, G.P., KUNZMANN, M., STRAUSS, J.V., AND MALOOF, A.C., 2018, The Tonian–Cryogenian transition in Northeastern Svalbard: *Precambrian Research*, v. 319, p. 79–95.

HOFFMAN, P.F., AND LI, Z.-X., 2009, A palaeogeographic context for Neoproterozoic glaciation: *Palaeogeography, Palaeoclimatology, Palaeoecology*, v. 277, p. 158–172.

HOFFMAN, P.F., HALVERSON, G.P., DOMACK, E.W., MALOOF, A.C., SWANSON-HYSELL, N.L., AND COX, G.M., 2012, Cryogenian glaciations on the southern tropical paleomargin of Laurentia (NE Svalbard and East Greenland), and a primary origin for the upper Russøya (Islay) carbon isotope excursion: *Precambrian Research*, v. 206–207, p. 137–158.

IMMONEN, N., 2013, Surface microtextures of ice-rafted quartz grains revealing glacial ice in the Cenozoic Arctic: *Palaeogeography, Palaeoclimatology, Palaeoecology*, v. 374, p. 293–302.

JACKSON, D.A., 1993, Stopping rules in principal components analysis: a comparison of heuristical and statistical approaches: *Ecology*, v. 74, p. 2204–2214.

JANITZKY, P., 1986, Laboratory methods: citrate–bicarbonate–dithionite (CBD) extractable iron and aluminum, in Singer, M.J., and Janitzky, P., eds., *Field and Laboratory Procedures Used in a Soil Chronosequence Study*: U.S. Geological Survey, Bulletin, p. 38–41.

JUNGBLUT, A.D., HAWES, I., MACKY, T.J., KRUSOR, M., DORAN, P.T., SUMNER, D.Y., EISEN, J. A., HILLMAN, C., and GORONCY, A.K., 2016, Microbial mat communities along an oxygen gradient in a perennially ice-covered Antarctic lake: *Applied and Environmental Microbiology*, v. 82, p. 620–630.

KALIŃSKA-NARTIŚA, E., LAMSTERS, K., KARUŠS, J., KRIEVĀNS, M., REČS, A., and MEIJA, R., 2017, Quartz grain features in modern glacial and proglacial environments: a microscopic study from the Russell Glacier, southwest Greenland: *Polish Polar Research*, v. 38, p. 265–289.

KEISER, L.J., SOREGHAN, G.S., and KOWALEWSKI, M., 2015, Use of quartz microtextural analysis to assess possible proglacial deposition for the Pennsylvanian–Permian Cutler Formation (Colorado, U.S.A.): *Journal of Sedimentary Research*, v. 85, p. 1310–1322.

KENDALL, B., CREASER, R.A., and SELBY, D., 2006, Re-Os geochronology of postglacial black shales in Australia: constraints on the timing of “Sturtian” glaciation: *Geology*, v. 34, p. 729.

KOCUREK, G., and FIELDER, G., 1982, Adhesion structures: *Journal of Sedimentary Petrology*, v. 52, p. 1229–1241.

KRINSLEY, D.H., and DOORNKAMP, J.C., 1973, *Atlas of Sand Grain Surface Textures*: Cambridge University Press, 102 p.

KRINSLEY, D.H., and FUNNELL, B.M., 1965, Environmental history of quartz sand grains from the Lower and Middle Pleistocene of Norfolk, England: *Geological Society of London, Quarterly Journal*, v. 121, p. 435–456.

KRINSLEY, D.H., and TAKAHASHI, T., 1962, Applications of electron microscopy to geology: *New York Academy of Sciences, Transactions*, p. 3–22.

KRINSLEY, D.H., and TRUSTY, P., 1985, Environmental interpretation of quartz grain surface textures, in Zuffa, G.G., ed., *Provenance of Arenites*: Dordrecht, Springer, p. 213–229.

KŘÍŽEK, M., KRBCOVÁ, K., MÍDA, P., and HANÁČEK, M., 2017, Micromorphological changes as an indicator of the transition from glacial to glaciofluvial quartz grains: evidence from Svalbard: *Sedimentary Geology*, v. 358, p. 35–43.

LEGENDRE, P., and LEGENDRE, L., 1998, *Numerical ecology*: Elsevier Science, 1006 p.

LEPPER, K., and SCOTT, G.F., 2005, Late Holocene aeolian activity in the Cimarron River valley of west-central Oklahoma: *Geomorphology*, v. 70, p. 42–52.

LINDÉ, K., and MYCIELSKA-DOWGIAŁŁO, E., 1980, Some experimentally produced microtextures on grain surfaces of quartz sand: *Geografiska Annalea*, v. 62, p. 171–184.

MACKY, T.J., SUMNER, D.Y., HAWES, I., JUNGBLUT, A.D., and ANDERSEN, D.T., 2015, Growth of modern branched columnar stromatolites in Lake Joyce, Antarctica: *Geobiology*, v. 13, p. 373–390.

MACKY, T.J., SUMNER, D.Y., HAWES, I., and JUNGBLUT, A.D., 2017, Morphological signatures of microbial activity across sediment and light microenvironments of Lake Vanda, Antarctica: *Sedimentary Geology*, v. 361, p. 82–92.

MAHANEY, W.C., 2002, *Atlas of Sand Grain Surface Textures and Applications*: Oxford University Press, 237 p.

MAHANEY, W.C., and KALM, V., 1995, Scanning electron microscopy of Pleistocene tills in Estonia: *Boreas*, v. 24, p. 13–29.

MAHANEY, W.C., and KALM, V., 2000, Comparative scanning electron microscopy study of oriented till blocks, glacial grains and Devonian sands in Estonia and Latvia: *Boreas*, v. 29, p. 35–51.

MAHANEY, W.C., CLARIDGE, G., and CAMPBELL, I., 1996, Microtextures on quartz grains in tills from Antarctica: *Palaeogeography, Palaeoclimatology, Palaeoecology*, v. 121, p. 89–103.

MAHANEY, W.C., STEWART, A., and VOLLI, K., 2001, Quantification of SEM microtextures useful in sedimentary environmental discrimination: *Boreas*, v. 30, p. 165–171.

MARGOLIS, S.V., and KRINSLEY, D.H., 1971, Submicroscopic frosting on eolian and subaqueous quartz sand grains: *Geological Society of America, Bulletin*, v. 82, p. 3395–3406.

MARGOLIS, S.V., and KRINSLEY, D.H., 1974, Processes of formation and environmental occurrence of microfeatures on detrital quartz grains: *American Journal of Science*, v. 274, p. 449–464.

NARTIŚA, M., and KALIŃSKA-NARTIŚA, E., 2017, An aeolian or a glaciolacustrine record? A case study from Mieļupīte, Middle Gauja Lowland, northeast Latvia: *Geologos*, v. 23, p. 15–28.

NIETER, W.M., and KRINSLEY, D.H., 1976, The production and recognition of aeolian features on sand grains by silt abrasion: *Sedimentology*, v. 23, p. 713–720.

PEDREGOSA, F., VAROQUAUX, G., and GRAMFORT, A., et al., 2011, Scikit-learn: machine learning in Python: *Journal of Machine Learning Research*, v. 12, p. 2825–2830.

PERES-NETO, P.R., JACKSON, D.A., and SOMERS, K.M., 2003, Giving meaningful interpretation to ordination axes: assessing loading significance in principal component analysis: *Ecology*, v. 84, p. 2347–2363.

PETTJOHN, F.J., 1957, *Paleocurrents of Lake Superior Precambrian quartzites*: Geological Society of America, Bulletin, v. 68, p. 469–480.

PIPPIN, M., 2016, Progressive downstream overprinting of glacially induced quartz microtextures during fluvial saltation, Salmon River, British Columbia and Alaska [MS Thesis]: Texas Tech University, 85 p.

PORTER, J.J., 1962, Electron microscopy of sand surface texture: *Journal of Sedimentary Petrology*, v. 32, p. 124–135.

PRAVE, A.R., CONDON, D.J., HOFFMANN, K.H., TAPSTER, S., and FALLICK, A.E., 2016, Duration and nature of the end-Cryogenian (Marinoan) glaciation: *Geology*, v. 44, p. 631–634.

PYE, K., 1983, Coastal dunes: *Progress in Physical Geography*, v. 7, p. 531–557.

PYE, K., and TSOAR, H., 2009, *Aeolian Sand and Sand Dunes*: Springer, 458 p.

ŘÍHA, K., KRUPKA, A., and COSTA, P.J.M., 2019, Image analysis applied to quartz grain microtextural provenance studies: *Computers & Geosciences*, v. 125, p. 98–108.

ROSE, C.V., MALOOF, A.C., SCHOENE, B., EWING, R.C., LINNEMANN, U., HOFMANN, M., and COTTLE, J.M., 2013, The end-Cryogenian glaciation of South Australia: *Geoscience Canada*, v. 40, p. 256.

RUNKEL, A.C., MACKY, T.J., COWAN, C.A., and FOX, D.L., 2010, Tropical shoreline ice in the late Cambrian: implications for Earth’s climate between the Cambrian Explosion and the Great Ordovician Biodiversification Event: *GSA Today*, v. 20, no. 11, p. 4–10.

SCHELP, C., 2019, An Alternative Way to Plot the Covariance Ellipse, at CarstenSchelp.github.io at [https://carstenschelp.github.io/2018/09/14/Plot\\_Confidence\\_Ellipse\\_001.html](https://carstenschelp.github.io/2018/09/14/Plot_Confidence_Ellipse_001.html).

SETLOW, L.W., 1978, Age determination of reddened coastal dunes in northwest Florida, U.S.A., by use of scanning electron microscopy, in Whalley, W.B., ed., *Scanning Electron Microscopy in the Study of Sediments*: *Geo Abstracts*, p. 283–305.

SHACAT, J.A., GREEN, W.J., DECARLO, E.H., and NEWELL, S., 2004, The Geochemistry of Lake Joyce, McMurdo Dry Valleys, Antarctica: *Aquatic Geochemistry*, v. 10, p. 325–352.

SMITH, C., SOREGHAN, G.S., and OHTA, T., 2018, Scanning electron microscope (SEM) microtextural analysis as a paleoclimate tool for fluvial deposits: a modern test: *Geological Society of America, Bulletin*, v. 130, p. 1256–1272.

SPIGEL, R.H., and PRISCU, J.C., 1998, Physical limnology of the McMurdo Dry Valleys Lakes, in *Ecosystem Dynamics in a Polar Desert: the McMurdo Dry Valleys, Antarctica*: American Geophysical Union, p. 153–187.

STEVIC, M., 2015, Identification and environmental interpretation of microtextures on quartz grains from aeolian sediments: Brattforsheden and Vittskövle, Sweden [BS Thesis]: Lund University, 35 p.

STOKES, S., KOCUREK, G., PYE, K., and WINSPEAR, N.R., 1997, New evidence for the timing of aeolian sand supply to the Algodones dunefield and East Mesa area, southeastern California, USA: *Palaeogeography, Palaeoclimatology, Palaeoecology*, v. 128, p. 63–75.

SWEET, D.E., and BRANNAN, D.K., 2016, Proportion of glacially to fluvially induced quartz grain microtextures along the Chitina River, SE Alaska, U.S.A.: *Journal of Sedimentary Research*, v. 86, p. 749–761.

SWEET, D.E., and SOREGHAN, G.S., 2010, Application of quartz sand microtextural analysis to infer cold-climate weathering for the equatorial Fountain Formation (Pennsylvanian–Permian, Colorado, U.S.A.): *Journal of Sedimentary Research*, v. 80, p. 666–677.

VINCENT, P.J., 1976, Some periglacial deposits near Aberystrwyth, Wales, as seen with a scanning electron microscope: *Bulletin Periglaciary*, v. 25, p. 59–64.

VOS, K., VANDENBERGHE, N., and ELSEN, J., 2014, Surface textural analysis of quartz grains by scanning electron microscopy (SEM): from sample preparation to environmental interpretation: *Earth-Science Reviews*, v. 128, p. 93–104.

WILLIAMS, G.E., 1998, Late Neoproterozoic periglacial aeolian sand sheet, Stuart Shelf, South Australia: *Australian Journal of Earth Sciences*, v. 45, p. 733–741.

WILSON, I.G., 1972, Aeolian bedforms: their development and origins: *Sedimentology*, v. 19, p. 173–210.

WINSPEAR, N.R., and PYE, K., 1995, Sand supply to the Algodones dunefield, south-eastern California, USA: *Sedimentology*, v. 42, p. 875–891.

WORONKO, B., 2016, Frost weathering versus glacial grinding in the micromorphology of quartz sand grains: processes and geological implications: *Sedimentary Geology*, v. 335, p. 103–119.

YU, W., ALGEO, T.J., DU, Y., ZHOU, Q., WANG, P., XU, Y., YUAN, L., and PAN, W., 2017, Newly discovered Sturtian cap carbonate in the Nanhua Basin, South China: *Precambrian Research*, v. 293, p. 112–130.

ZHANG, S., JIANG, G., and HAN, Y., 2008, The age of the Nantuo Formation and Nantuo glaciation in South China: *Terra Nova*, v. 20, p. 289–294.

Received 24 September 2020; accepted 2 June 2021.